

1 **Computing Rates and Distributions of Rock Recovery**
2 **in Subduction Zones**

3 **Buchanan C. Kerswell** ¹**Matthew J. Kohn** ²**Taras V. Gerya** ³

4 ¹Department of Geology & Environmental Earth Science, Miami University, Oxford, OH 45056

5 ²Department of Geosciences, Boise State University, Boise, ID 83725

6 ³Department of Earth Sciences, ETH-Zurich, Sonneggstrasse 5, Zurich 8092, Switzerland

7 **Key Points:**

- 8 • Simulated rocks detach at depths consistent with major mechanical transitions along
9 subduction interfaces
- 10 • Simulated rock PT distributions and recovery rates correlate with boundary con-
11 ditions
- 12 • Few simulated rocks detach from the PT region of highest natural sample density

Abstract

Bodies of rock that are detached (recovered) from subducting oceanic plates, and exhumed to Earth's surface, become invaluable records of the mechanical and chemical processing of rock along subduction interfaces. Exposures of interface rocks with high-pressure (HP) mineral assemblages provide insights into the nature of rock recovery, yet various interpretations concerning thermal gradients, recovery rates, and recovery depths arise when directly comparing the rock record with numerical simulations of subduction. Constraining recovery rates and depths from the rock record presents a major challenge because small sample sizes of HP rocks makes statistical inference weak. As an alternative approach, this study implements numerical simulations of oceanic-continental convergence and applies a classification algorithm to identify rock recovery. Over one million markers are classified from 64 simulations representing a large range of subduction zones. We find recovery P's (depths) correlate strongly with convergence velocity and moderately with oceanic plate age, while PT gradients correlate strongly with oceanic plate age and upper-plate thickness. Recovery rates strongly correlate with upper-plate thickness, yet show no correlation with other boundary conditions. Likewise, PT distributions of recovered markers vary among numerical experiments and generally show poor overlap with the rock record. A significant gap in predicted marker recovery is found near 2 GPa and 550 °C, coinciding with the highest density of exhumed HP rocks. Implications for such a gap in marker recovery include numerical modeling uncertainties, petrologic uncertainties, selective sampling of exhumed HP rocks, or natural geodynamic factors not accounted for in numerical experiments.

Plain language summary

Converging tectonic plates leads to subduction of the denser plate beneath the other. Bodies of subducted rock that return to Earth's surface bring information about the deep subduction interface, yet the rates, depths, and mechanisms that detach rock from the subducting plate are not well-understood. As an alternative to studying rock samples, this study implements a machine learning algorithm to identify rock detachment in numerical simulations. Over one million simulated rocks are classified from 64 simulations representing a large range of possible subduction zones. Marker pressure-temperature (PT) conditions are compared across models and with the rock record. Correlations are drawn among important model parameters, including plate velocities and plate thick-

ness, that reveal strong and weak effects on marker detachment. Recovery rates strongly correlate with upper-plate thickness, yet show no correlation with other parameters. Likewise, PT distributions of markers show variable compatibility with the rock record depending on the comparison. A significant gap marker recovery coincides with a large proportion of exhumed HP rocks. Implications for such a gap in marker recovery include numerical modeling uncertainties, petrologic uncertainties, selective sampling of exhumed HP rocks, or natural geodynamic factors not accounted for in numerical experiments.

1 Introduction

Maximum pressure-temperature (PT) conditions have been estimated for hundreds of high-pressure (HP) metamorphic rocks exhumed from subduction zones (Figure 1, Agard et al., 2018; Hacker, 1996; Penniston-Dorland et al., 2015). These samples represent fragments of oceanic crust, continental crust, seafloor sediments, and upper mantle that have detached from subducting oceanic and continental lithospheres at various depths along the interface between subducting and overriding tectonic plates (referred to as “recovery” after Agard et al. (2018)). This *rock record* is the only tangible evidence of PT-strain fields, deep seismic cycling, and fluid flow within Earth’s lithosphere during deformation and chemical processing in subduction zones. Together with geophysical imaging (e.g. Bostock, 2013; Ferris et al., 2003; Hyndman & Peacock, 2003; Mann et al., 2022; Naif et al., 2015; Rondenay et al., 2008; Syracuse & Abers, 2006), analysis of surface heat flow data (e.g. Currie & Hyndman, 2006; Gao & Wang, 2014; Hyndman et al., 2005; Kohn et al., 2018; Morishige & Kuwatani, 2020; Wada & Wang, 2009), and forward numerical geodynamic modeling (e.g. Gerya et al., 2002, 2008; Gerya & Stöckhert, 2006; Hacker et al., 2003; Kerswell et al., 2021; McKenzie, 1969; Peacock, 1990, 1996; Sizova et al., 2010; Syracuse et al., 2010; Yamato et al., 2007, 2008), investigation of the rock record underpins contemporary understandings of subduction geodynamics (e.g. Agard et al., 2009; Agard, 2021; Bebout, 2007).

However, it remains difficult to directly interpret the rock record in terms of recovery rates and distributions along the subduction interface. For example, compilations of PT estimates representing the global distribution of HP rocks exhumed during the Phanerozoic (the pd15 and ag18 datasets, Agard et al., 2018; Penniston-Dorland et al., 2015) reveal an abrupt decrease in relative sample abundance at P’s above 2.3-2.4 GPa (Figure 1). For pd15 and ag18, a nearly-constant cumulative distribution (CDF) curve interrupted

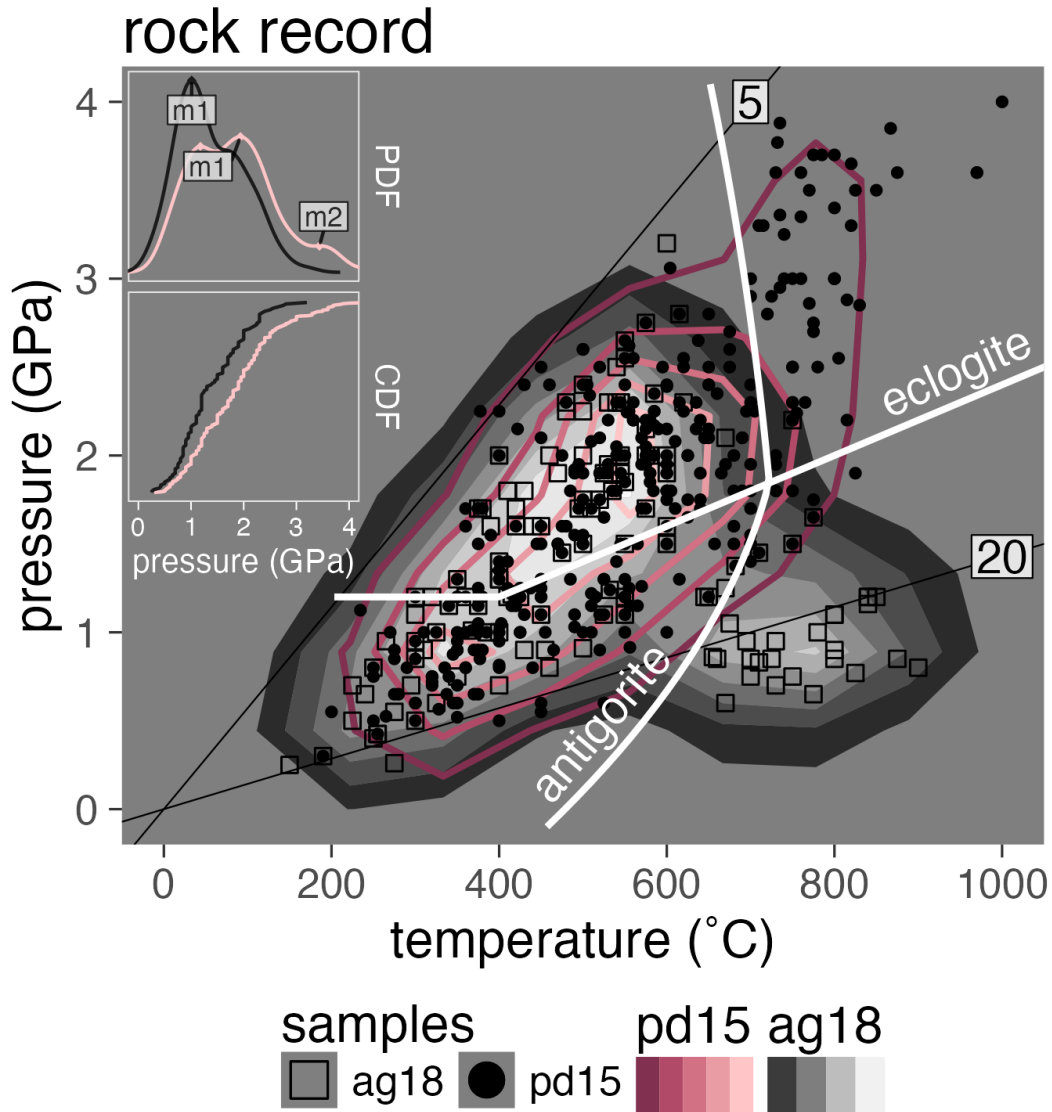


Figure 1: PT diagram showing distributions of PT estimates for exhumed HP metamorphic rock samples compiled in the pd15 (solid contours, Penniston-Dorland et al., 2015) and ag18 (filled contours, Agard et al., 2018) datasets. (insets) Probability distribution diagrams of pd15 and ag18 samples showing broad bimodal and trimodal sample distributions with respect to P (top inset) and a kinked CDF (bottom inset) indicating that a substantial proportion of markers are recovered from P's between 0.5-2.5 GPa with very few rocks reaching maximum P's above 3 GPa. Thin lines are thermal gradients labeled in $^{\circ}$ C/km. Reaction boundaries for eclogitization of oceanic crust and antigorite dehydration are from Ito & Kennedy (1971) and Schmidt & Poli (1998), respectively.

77 by a sharp change in slope around 2.3-2.4 GPa implies relatively uniform recovery of sub-
78 ducting material up to 2.3-2.4 GPa, but increasingly rare recovery above 2.3-2.4 GPa (Agard
79 et al., 2018; Kerswell et al., 2021; Monie & Agard, 2009; Plunder et al., 2015). On the
80 one hand, evidence for common mechanical coupling depths near 2.3 GPa (Furukawa,
81 1993; Kerswell et al., 2021; Wada & Wang, 2009) suggests an upper-limit to recovery depths
82 that is consistent with the scarcity of (ultra-)HP samples in the rock record and invari-
83 ant with respect to key thermo-kinematic parameters (convergence velocity, subduction
84 geometry, plate thickness; Figure 1). On the other hand, substantial variations in lat-
85 eral (along-strike) upper-plate surface heat flow patterns suggest coupling depths also
86 vary substantially among subduction zone segments (Kerswell & Kohn, 2022) and do im-
87 pose an invariant upper-limit to recovery depths. Moreover, geophysical constraints on
88 the depths of key mechanical transitions likely to induce rock recovery (e.g. Abers et al.,
89 2020; Audet & Kim, 2016; Audet & Schaeffer, 2018; Morishige & Kuwatani, 2020) sug-
90 gest high recovery rates should cluster around discrete depths, rather than uniform and
91 widespread recovery along the subduction interface implied by the pd15 and ag18 datasets.

92 Difficulties in relating complex polymetamorphic rocks from different environments
93 challenge the use of PT distributions of exhumed HP rock samples as robust constraints
94 on key subduction zone parameters. Interpretations of rock recovery mechanisms, sub-
95 duction interface behavior, metamorphic reactions, seismic cycling, and subduction geo-
96 dynamics might vary depending on metamorphic terrane (local tectonic environment),
97 sampling strategy (random or targeted outcrops), sample size (how many outcrops were
98 observed and sampled in the field), and analytical sample selection (investigating PT's
99 and deformation histories for a subset of samples with a specific scientific question in mind).
100 Different compilations of PT estimates can show different density distributions, in terms
101 of relative abundances of samples across PT space, and thus imply different depths of
102 rock recovery along the subduction interface. For example, Agard et al. (2018) noted
103 that compilations from Plunder et al. (2015) and Groppo et al. (2016) show less disper-
104 sion (i.e. a more step-like CDF) than ag18 with tighter bimodal or trimodal distributions
105 clustering around inferred depths of important mechanical transitions along the subduc-
106 tion interface. These peaks (modes) in distributions of exhumed HP rocks coincide with
107 the continental Moho at approximately 25-35 km and the transition to mechanical plate
108 coupling at approximately 80 km (Agard et al., 2018; Monie & Agard, 2009; Plunder et
109 al., 2015). Less consensus explains a smaller, yet significant, intermediate mode at 55-

110 60 km (Agard et al., 2009, 2018; Plunder et al., 2015), although it is consistent with a
111 high- density region of PT estimates in the pd15 dataset.

112 Differences in compiled PT datasets notwithstanding, key observations regarding
113 rock recovery in subduction zones emerge from pd15 and ag18:

- 114 1. Rocks are recovered with relatively similar frequency up to 2.5 GPa
- 115 2. 64-66% of recovered rocks equilibrated between 1-2.5 GPa
- 116 3. 5-19% of recovered rocks equilibrated above 2.5 GPa
- 117 4. 32-34% of recovered rocks equilibrated between 350-525 °C
- 118 5. 50-56% of recovered rocks equilibrated above 525 °C
- 119 6. 52-62% of recovered rocks record gradients between 5-10 °C/km
- 120 7. 18-31% of recovered rocks record gradients between 10-15 °C/km
- 121 8. 6-30% of recovered rocks record gradients above 15 °C/km

122 These ranges in the relative abundances of exhumed HP rocks compiled in different datasets
123 raise important questions in subduction zone research: are rocks recovered broadly and
124 uniformly along the subduction interface or discretely from certain depths? How do re-
125 covery rates and distributions vary among diverse subduction zone settings and through
126 time?

127 Previous work comparing the rock record directly with numerical models has gen-
128 erally produced ambiguous interpretations concerning recovery rates and distributions
129 along the subduction interface. For example, comparisons of different numerical geody-
130 namic codes with subsets of the rock record show variable agreement in terms of over-
131 lapping PT paths and thermal gradients (e.g. Angiboust et al., 2012b; Burov et al., 2014;
132 Holt & Condit, 2021; Penniston-Dorland et al., 2015; Plunder et al., 2018; Roda et al.,
133 2010, 2012, 2020; Ruh et al., 2015; Yamato et al., 2007, 2008). Initial setups for numer-
134 ical experiments (oceanic plate age, convergence velocity, subduction dip angle, upper-
135 plate thickness, and heating sources; Kohn et al., 2018; Penniston-Dorland et al., 2015;
136 Ruh et al., 2015; van Keken et al., 2019), differential recovery rates from subduction zones
137 with favorable thermo-kinematic boundary conditions (Abers et al., 2017; van Keken et
138 al., 2018), and comparisons among suites of undifferentiated HP rocks (e.g. grouping rocks
139 recovered during subduction initiation with rocks recovered during “steady-state” sub-
140 duction, see Agard et al., 2018, 2020) all potentially contribute to nonoverlapping PT

141 distributions and thermal gradients between exhumed HP rocks and numerical geody-
142 namic models. Compounding the ambiguity are arguments that material is sporadically
143 recovered during short-lived mechanical transitions (Agard et al., 2016) and/or geody-
144 namic changes (Monie & Agard, 2009)—implying exhumed HP rocks are not random
145 samples of the subduction interface during steady-state subduction. Such ambiguities
146 warrant further investigation into the general response of recovery rates and distribu-
147 tions to broad ranges of thermo-kinematic boundary conditions and various implemen-
148 tations of subduction interface rheologies.

149 Fortunately, clues about the nature and PT limits of rock recovery are provided
150 by many extensively studied examples of exhumed subduction interfaces (e.g. Agard et
151 al., 2018; Angiboust et al., 2011; 2015; Cloos & Shreve, 1988; Fisher et al., 2021; Ioan-
152 nidi et al., 2020; Kitamura & Kimura, 2012; Kotowski & Behr, 2019; Locatelli et al., 2019;
153 Monie & Agard, 2009; Okay, 1989; Platt, 1986; Plunder et al., 2013, 2015; Tewksbury-
154 Christle et al., 2021; Wakabayashi, 2015). However, these type localities represent an un-
155 known fraction of subducted material and differ significantly in terms of their geome-
156 try (field relationships), composition (rock types), and interpreted deformation histories
157 (both detachment and exhumation). It is also unclear to what extent ag18 and pd15 (and
158 other compilations) represent the full range of recovery conditions and/or represent sci-
159 entific sampling bias (e.g. undersampling low-grade rocks or oversampling high-grade rocks
160 from the same pristine exposures, Agard et al., 2018). Thus, a primary challenge to in-
161 ferring recovery rates and distributions accurately from the rock record fundamentally
162 stems from sparse nonrandom samples (typically less than a few dozen PT estimates from
163 any given exhumed terrane) compared to the diversity of thermo-kinematic parameters
164 characterizing subduction zones and petro-thermo-mechanical conditions suitable for rock
165 recovery along the subduction interface.

166 This study aims at addressing the sparsity and nonrandomness of exhumed HP rock
167 samples by tracing numerous (1,341,729) Lagrangian markers from 64 numerical geody-
168 namic simulations of oceanic-continental subduction (Kerswell et al., 2021). We first gen-
169 erate a PT dataset from instantiations of a particular numerical geodynamic code so large
170 that it was insensitive to noise and outliers—thus representing a statistically robust pic-
171 ture of recovery rates and PT distributions in subduction zones. From such a large dataset
172 of generated samples, we identify correlations among recovery rates, PT distributions,
173 and thermo-kinematic boundary conditions that quantify parameter sensitivities and in-

174 dicate ranges of plausible conditions for reproducing the rock record. In fact, surpris-
175 ingly low densities of generated samples, in terms of their relative abundances across PT
176 space, were found coinciding with the highest-density regions of natural samples around
177 2 GPa and 550 °C. We then discuss implications for poor overlap between generated sam-
178 ple densities and exhumed HP rock densities, including insufficient implementation of
179 recovery mechanisms in numerical geodynamic models (numerical bias) and a potential
180 overabundance of natural samples collected from similar metamorphic grades around 2
181 GPa and 550 °C (empirical bias).

182 **2 Methods**

183 This study presents a dataset of Lagrangian markers (described below) from nu-
184 merical experiments that simulated 64 oceanic-continental convergent margins with thermo-
185 kinematic boundary conditions (oceanic plate age, convergence velocity, and upper-plate
186 lithospheric thickness) closely representing the range of presently active subduction zones
187 (Syracuse & Abers, 2006; Wada & Wang, 2009). Initial conditions were modified from
188 previous studies of active margins (Gorczyk et al., 2007; Sizova et al., 2010) using the
189 numerical geodynamic code I2VIS (Gerya & Yuen, 2003). I2VIS models visco-plastic flow
190 of geological materials by solving conservative equations of mass, energy, and momen-
191 tum on a fully-staggered finite difference grid with a *marker-in-cell* technique (Gerya,
192 2019; Gerya & Yuen, 2003; e.g. Harlow & Welch, 1965). Complete details about the ini-
193 tial setup, boundary conditions, and rheological model are presented in Kerswell et al.
194 (2021). Complete details about I2VIS and example code are presented in Gerya & Yuen
195 (2003) and Gerya (2019).

196 The following section defines Lagrangian markers (now referred to as *markers*) and
197 briefly elaborates on their usefulness in understanding flow of geological materials, fol-
198 lowed by a description of the marker classification algorithm. A complete mathemati-
199 cal description of the classification algorithm is presented in Appendix A.1.

200 **2.1 Lagrangian Markers**

201 Markers are mathematical objects representing discrete parcels of material flow-
202 ing in a continuum (Harlow, 1962, 1964). Tracing markers (saving marker information

at each timestep) is distinctly advantageous for investigating subduction dynamics in the following two ways.

First, modeling subduction requires solving equations of mass, motion, and heat transport in a partly layered, partly heterogeneous, high-strain region known as the *plate interface*, *subduction interface*, or *subduction channel* (Gerya et al., 2002). Current conceptual models regard the subduction interface as a visco-plastic continuum with complex geometry and structure, sharp thermal, chemical, and strain gradients, strong advection, and abundant fluid flow (Agard et al., 2016, 2018; Bebout, 2007; Bebout & Barton, 2002; Cloos & Shreve, 1988; Gerya & Yuen, 2003; Penniston-Dorland et al., 2015; Shreve & Cloos, 1986; Stöckhert, 2002; Tewksbury-Christle et al., 2021). Finite-difference numerical approaches do not perform well with strong local gradients, and interpolating and updating T, strain, and chemical fields with markers greatly improves accuracy and stability of numerical solutions (Gerya, 2019; Gerya & Yuen, 2003; Moresi et al., 2003).

Second, tracing a marker closely proxies for tracing a rock’s PT-time history. Strictly speaking, deviations between calculated PT-time histories of markers and rocks are possible because our numerical geodynamic simulations assume: (1) markers move in an incompressible continuum (Batchelor, 1953; Boussinesq, 1897), (2) material properties are governed by a simplified petrologic model describing eclogitization of oceanic crust (Ito & Kennedy, 1971) and (de)hydration of upper mantle ($\text{antigorite} \Leftrightarrow \text{olivine} + \text{orthopyroxene} + \text{H}_2\text{O}$, Schmidt & Poli, 1998), and (3) marker stress and strain are related by a highly non-linear rheological model derived from empirical flow laws (Hilaret et al., 2007; Karato & Wu, 1993; Ranalli, 1995; Turcotte & Schubert, 2002). For example, if rocks within a subduction interface shear zone were highly compressible or could sustain large deviatoric stresses, P’s and T’s might be different from markers. The hydrological model implemented in our numerical simulations, embodied by assumptions 2 and 3, exert particularly strong control on subduction interface strength, and thus the probability and style of detachment. Our simulations developed stable subduction channels (tectonic-mélanges, e.g. Gerya et al., 2002) instead of discrete shear zones that detach large coherent slices of oceanic lithosphere (e.g. Ruh et al., 2015) primarily due to our choice of hydrological model. However, insofar as subduction interface shear zones closely behave as mélange-like channels of incompressible visco-plastic fluids (under the assumptions above, Gerya, 2019; Gerya & Yuen, 2003; Kerswell et al., 2021), comparisons between marker PT distributions and the rock record may be made.

2.2 Marker Classification

For each numerical experiment, 20,986 markers were initially selected from within a 760 km-long and 8 km-deep section of oceanic crust and seafloor sediments at $t = 0$ Ma. Tracing proceeded for 115 timesteps (between 9.3-54.7 Ma depending on convergence velocity), which was sufficient for markers to be potentially subducted very deeply (up to 300 km) from their initial positions. However, only markers that detached from the subducting oceanic plate were relevant for comparison with PT estimates of exhumed HP rocks (because these markers and rocks were not subducted). The main challenge, therefore, was to first develop a method for determining which markers among 20,986 detached and moved away from the subducting plate without knowing their fate *a priori*. Moreover, the method needed to be generalizable to a large range of numerical experiments. Note that detached markers were classified as “recovered” even if they did not exhume to the surface within the modeling domain. Diverse processes can cause exhumation of subduction zone rocks, including later tectonic events, and our goal was to compare only the maximum metamorphic conditions of markers and rocks along their prograde paths.

Classifying unlabelled markers as either “recovered” or “not recovered” based solely on their undifferentiated traced histories defines an unsupervised classification problem (Barlow, 1989). Many methods can be applied to solve the unsupervised classification problem, yet this study implemented a Gaussian mixture model (Reynolds, 2009)—a type of “soft” clustering algorithm used extensively for pattern recognition, anomaly detection, and estimating complex probability distribution functions (e.g. Banfield & Raftery, 1993; Celeux & Govaert, 1995; Figueiredo & Jain, 2002; Fraley & Raftery, 2002; Vermeesch, 2018). “Hard” classification is possible by directly applying simple rules to markers without clustering (e.g. Roda et al., 2012). However, “hard” methods are less generalizable than “soft” approaches like Gaussian mixture models, which can be implemented to study many possible features in numerical simulations with Lagrangian reference frames—not just recovery of subducted material. In this case, a Gaussian mixture model organized markers into groups (clusters) by fitting $k = 14$ bivariate Gaussian ellipsoids to the distribution of markers in PT space. “Fitting” refers to adjusting parameters (centroids and covariance matrices) of all k Gaussian ellipsoids until the ellipsoids and data achieved maximum likelihood (see Appendix A.1 for a complete mathematical description). Fi-

268 nally, marker clusters with centroids located within certain bounds were classified as “re-
269 covered”. The entire classification algorithm can be summarized as follows:

- 270 0. Select markers within a 760 km \times 8 km section of oceanic crust
- 271 1. Trace markers for 115 timesteps
- 272 2. Identify maximum marker PT conditions (at either maxT or maxP)
- 273 3. Apply Gaussian mixture modeling to maximum marker PT conditions
- 274 4. Check for cluster centroids within the bounds:
 - 275 • ≥ 3 °C/km AND
 - 276 • ≤ 1300 °C AND
 - 277 • ≤ 120 km (3.4 GPa)
- 278 5. Classify marker clusters found in step 4 as “recovered”
- 279 6. Classify all other markers as “not recovered”

280 Note that maximum marker PT conditions used for clustering were assessed before mark-
281 ers transformed (dehydrated or melted) and before the accretionary wedge toe collided
282 with the high-viscosity convergence region positioned at 500 km from the left boundary
283 (to avoid spurious maximum PT conditions from sudden isothermal burial). We also tried
284 applying different prograde PT path positions in step 2 by determining maximum marker
285 T’s (maxT) and maximum P’s (maxP) independently. Applying maxP vs. maxT con-
286 ditions to the classifier resulted in distinct PT distributions of recovered markers and
287 distinct correlations among thermo-kinematic boundary conditions and marker recov-
288 ery modes. For natural samples of exhumed HP rocks, compilations emphasize maxP,
289 not maxT, (Penniston-Dorland et al., 2015), and thus empirical PT estimates are best
290 compared with maxP conditions. Also, many PT paths for exhumed HP rocks have “hair-
291 pin” or isothermal decompression retrograde PT paths without significant heating dur-
292 ing exhumation (Agard et al., 2009). Figures 2 & 3 illustrate marker classification for
293 1 of 64 numerical experiments. All other experiments are presented in Supplementary
294 ??.

295 **2.3 Recovery Modes**

296 To better quantify how rock recovery can vary among subduction zones with dif-
297 ferent boundary conditions, marker recovery modes (density peaks) were determined with

298 respect to absolute PT and PT gradients. The highest-density peak (mode1) shows where
299 the greatest abundance of markers are recovered. The deepest, or warmest, density peak
300 (mode2) shows where the most deeply subducted markers (or markers with the highest
301 PT gradients) are recovered. In other words, changes in the positions of mode1 and mode2
302 reflect variations in recovery conditions for “normal” recovery and “extreme cases”, re-
303 spectively.

304 Note that correlations are not presented here with respect to the thermal param-
305 eter Φ ($\Phi = \text{oceanic plate age} \cdot \text{convergence velocity}$), unlike many studies. The ration-
306 ale is three-fold: (1) the aim was to understand how oceanic plate age and convergence
307 velocity affect marker recovery independently, (2) sample sizes of recovered markers were
308 larger when grouped by oceanic plate age and convergence velocity ($n = 335,788$) com-
309 pared to grouping by Φ ($n = 83,947$; implying they do not correlate well with Φ), and
310 (3) and combining oceanic plate age and convergence velocity can draw unnecessarily
311 ambiguous associations with other geodynamic features of subduction zones (e.g. Φ vs. H
312 from England et al., 2004; Wada & Wang, 2009).

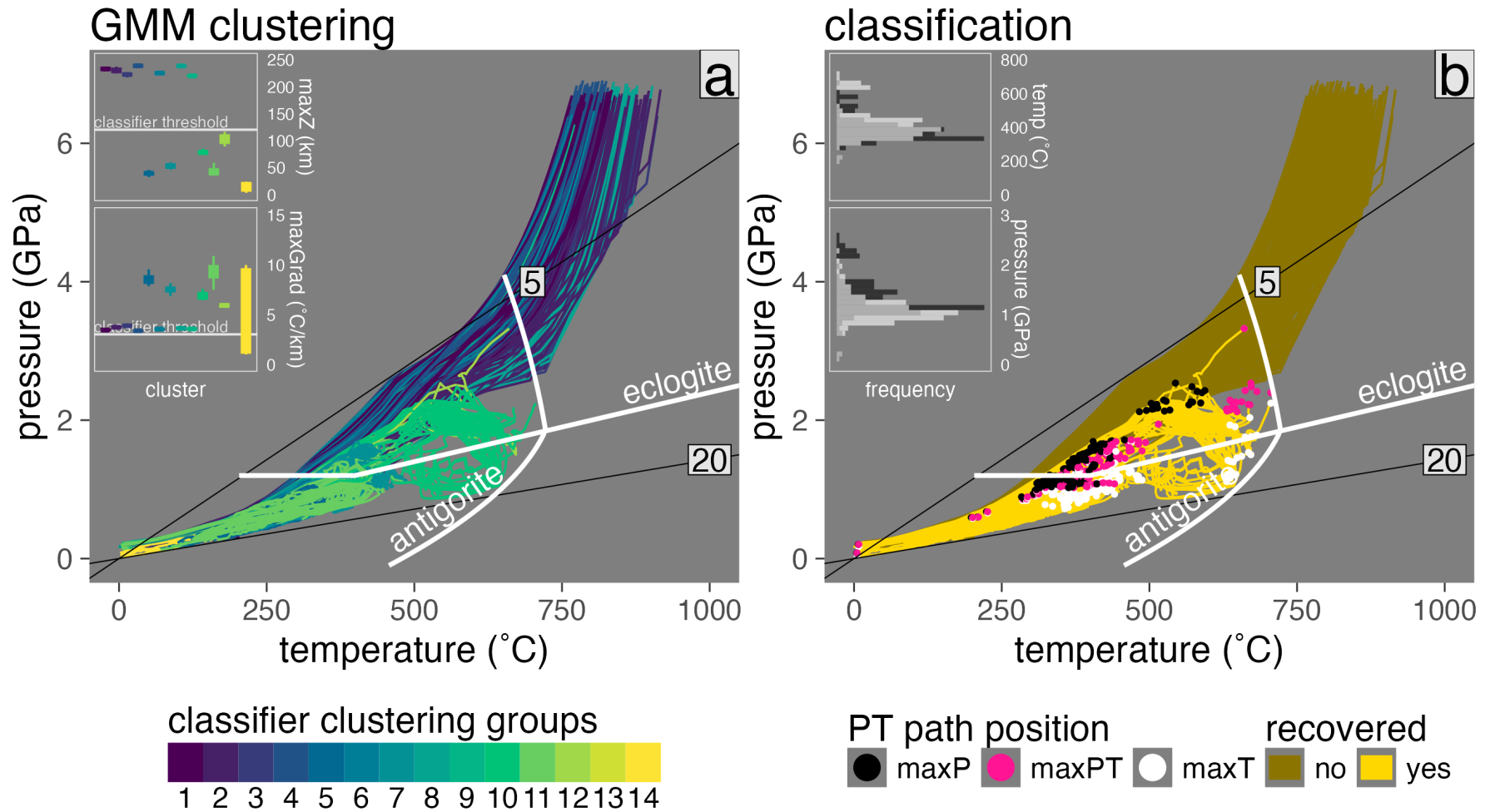


Figure 2: Example of marker classification for model cda62. (a) PT diagram showing marker clusters as assigned by Gaussian mixture modeling (GMM; colored PT paths). Boxplots showing depth and thermal gradient distributions of marker clusters assigned by GMM. Markers belonging to clusters with centroids (means) positioned at ≤ 120 km (top inset) and ≥ 5 °C/km (bottom inset) are classified as recovered. All others are classified as not recovered. (b) PT diagram showing marker classification results (colored PT paths) and various marker positions along their PT paths (black, white, and pink points). (insets) Histograms showing the distribution of T's (top inset) and P's (bottom inset) for recovered markers at maxP (black bars) and maxT (white bars) conditions. In this experiment, a significant number of markers have different peak metamorphic conditions between their maxT and maxP positions. Thin lines are thermal gradients labeled in °C/km. Only a random subset of markers are shown.

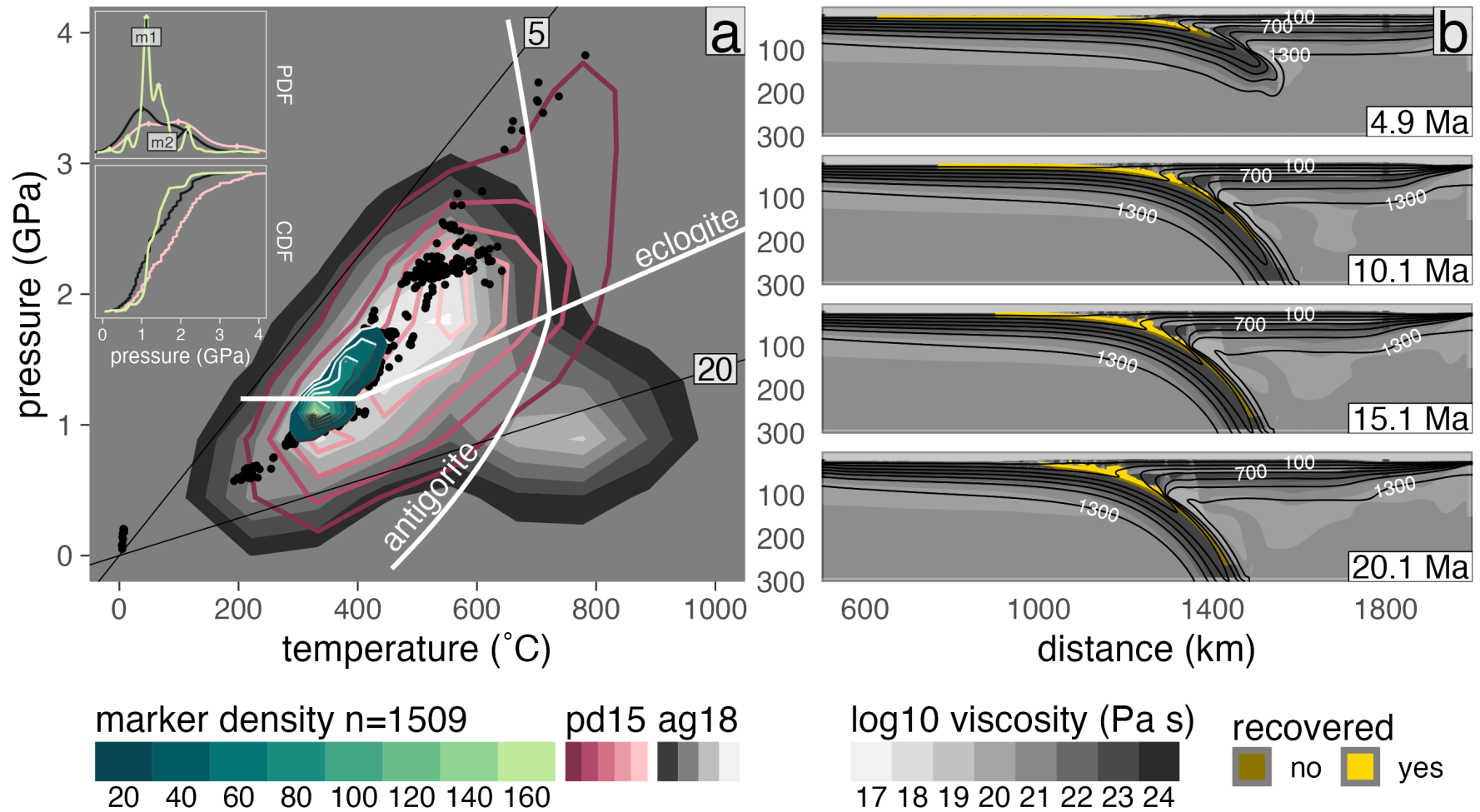


Figure 3: Summary of marker recovery for model cda62. (a) PT diagram showing the density of recovered markers (black points and green Tanaka contours) in comparison with the pd15 (solid red density contours) and ag18 (filled gray density contours) datasets. (insets) Probability distribution diagrams showing trimodal recovery P's (top inset) and a step-like CDF (bottom inset) indicating that a substantial proportion of markers are recovered from depths between 0.5-1.5 GPa. Thin lines are thermal gradients labeled in $^{\circ}\text{C}/\text{km}$. Reaction boundaries for eclogitization of oceanic crust and antigorite dehydration are from Ito & Kennedy (1971) and Schmidt & Poli (1998), respectively. (b) Visualization of log viscosity in the model domain showing the major modes of marker recovery along a relatively thick subduction interface that tapers near the viscous coupling depth.

3 Results

3.1 Comparing Marker PT Distributions with the Rock Record

3.1.1 Global Markers from all Numerical Experiments

While marker recovery can occur at all P's recorded by exhumed metamorphic rocks (Figure 4), large disparities between recovered markers and the rock record are found if considering sample densities with respect to P. For example, pd15 and ag18 show high sample densities centered at 1 GPa—a shared feature common to all 64 numerical experiments—yet sample densities above 1 GPa are much greater in pd15 and ag18 compared to simulations (relative to the total number of samples in each dataset; Figure 4). Samples compiled in pd15 and ag18 also show much broader bimodal or trimodal density distributions across P's compared to a narrow and strong unimodal P distribution centered at 1 GPa for recovered markers. With respect to T, thermal gradients of recovered markers are significantly lower than natural samples. On average, markers recovered from < 2 GPa differ by 173 °C and 3-4 °C/km compared to rocks exhumed from < 2 GPa (excluding the highest-T samples in ag18 that relate to subduction initiation, Agard et al., 2018, 2020; Soret et al., 2022). In fact, relatively poor overlap exists between the high-density peak of recovered markers centered at 1 GPa & 300° C and either high-density peaks of natural sample centered at 1 GPa & 350° C and 2 GPa & 550° C (Figure 4).

3.1.2 Markers from Individual Numerical Experiments

For most experiments, marker recovery is localized and discrete with peaky multimodal density distributions and step-like CDFs. The PT positions of recovery cluster centroids depend on thermo-kinematic boundary conditions, however, so marker PT distributions vary. A few experiments show broad marker distributions that resemble the rock record with respect to P, but not with respect to thermal gradients (Supplementary ??). Other experiments show the opposite. To compare marker recovery among various subduction zone settings, we combined recovered markers from multiple numerical experiments with similar thermo-kinematic boundary conditions—analogue to randomly sampling exhumed HP rocks from similar subduction zones (Figures 5 & 6).

341 Whether comparing the rock record with recovered markers from individual nu-
 342 merical experiments, suites of experiments, or all numerical experiments, several key ob-
 343 servations emerge (Figure 4):

- 344 1. Recovered markers from most individual numerical experiments show discrete mul-
 345 timodal PT distributions with steep step-like CDFs (Figure 3 & Supplementary
 346 ??)
- 347 2. Relatively few markers are recovered from PT regions coinciding with high-densities
 348 of natural samples around 2 GPa and 550 °C
- 349 3. Markers are recovered from a single major P mode near 1 GPa and minor P mode
 350 near 2.5 GPa with a higher rate of recovery from lower P's (79% from ≤ 1.5 GPa)
 351 compared to natural samples (36-59% from ≤ 1.5 GPa)
- 352 4. Markers are recovered from a single major T mode near 300 °C and minor T mode
 353 near 525 °C with a higher rate of recovery from lower T's (97% from ≤ 525 °C)
 354 compared to natural samples (44-50% from ≤ 525 °C)
- 355 5. The relative abundance of markers recovered along “typical” thermal gradients
 356 for subduction zones (87% from 5-12 °C/km) is high compared to natural sam-
 357 ples (59-78% from 5-12 °C/km)
- 358 6. Many markers are recovered from the forbidden zone (11% from ≤ 5 °C/km)
- 359 7. Virtually no markers (0.002%) are recovered from ≥ 15 °C/km compared to nat-
 360 ural samples (6-30% from ≥ 15 °C/km, Figure 4)

361 **3.2 Correlations with Boundary Conditions**

362 **3.2.1 Oceanic Plate Age Effect**

363 Thermal gradients of recovered markers respond strongly to changes in oceanic plate
 364 age (Figure 7, Table 1). Both PT gradient modes are strongly inversely correlated with
 365 oceanic plate age, showing a mean increase from about 5.88 ± 0.17 °C/km (Grad mode1)
 366 and 6.91 ± 0.68 °C/km (Grad mode2) for older plates (≥ 85 Ma) to about 7.25 ± 0.05
 367 °C/km (Grad mode1) and 8.84 ± 0.56 °C/km (Grad mode2) for younger plates (≤ 55
 368 Ma). The dominant P mode (P mode1) moderately correlates with oceanic plate age,
 369 indicating a slightly higher possibility of recovering material from beyond the continen-
 370 tal Moho for the oldest oceanic plates (≥ 85 Ma). Neither T modes, nor recovery rate

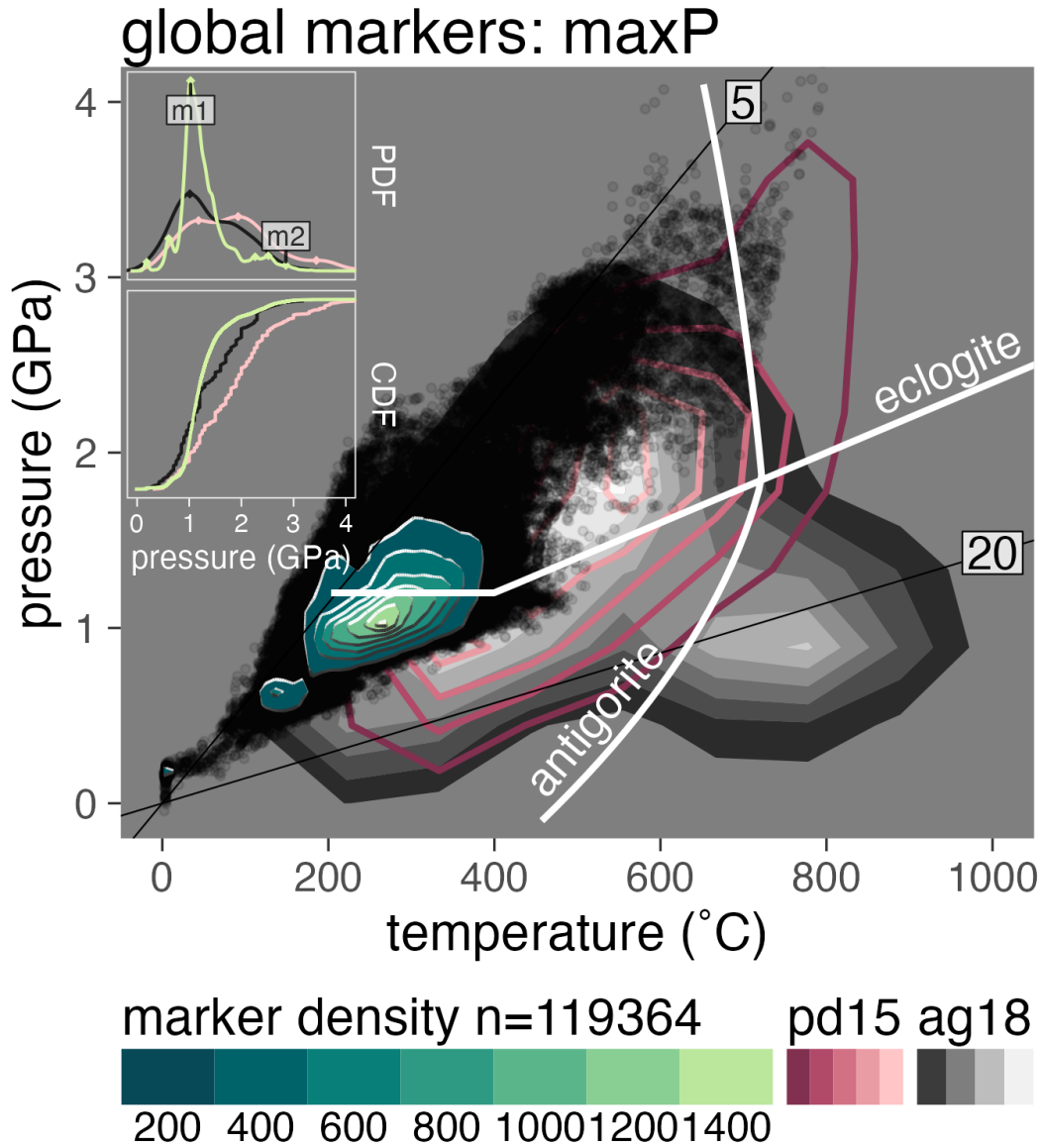


Figure 4: Recovered markers from all 64 numerical experiments. (a) PT diagram showing the density of recovered markers (black points and green Tanaka contours) in comparison with the pd15 (solid red density contours) and ag18 (filled gray density contours) datasets. Marker density is concentrated along relatively cool thermal gradients, primarily near the continental Moho (1 GPa), with minor recovery modes centered near the onset of plate coupling (2.3-2.5 GPa). (insets) Probability distribution diagrams showing discrete multimodal recovery P's (top inset) and a steep CDF (bottom inset) indicating that a substantial proportion of markers are recovered from depths between 0.5-1.5 GPa. Note the higher-abundance of pd15 and ag18 samples at > 1.5 GPa compared to markers. Thin lines are thermal gradients labeled in $^{\circ}\text{C}/\text{km}$. Reaction boundaries for eclogitization of oceanic crust and antigorite dehydration are from Ito & Kennedy (1971) and Schmidt & Poli (1998), respectively.

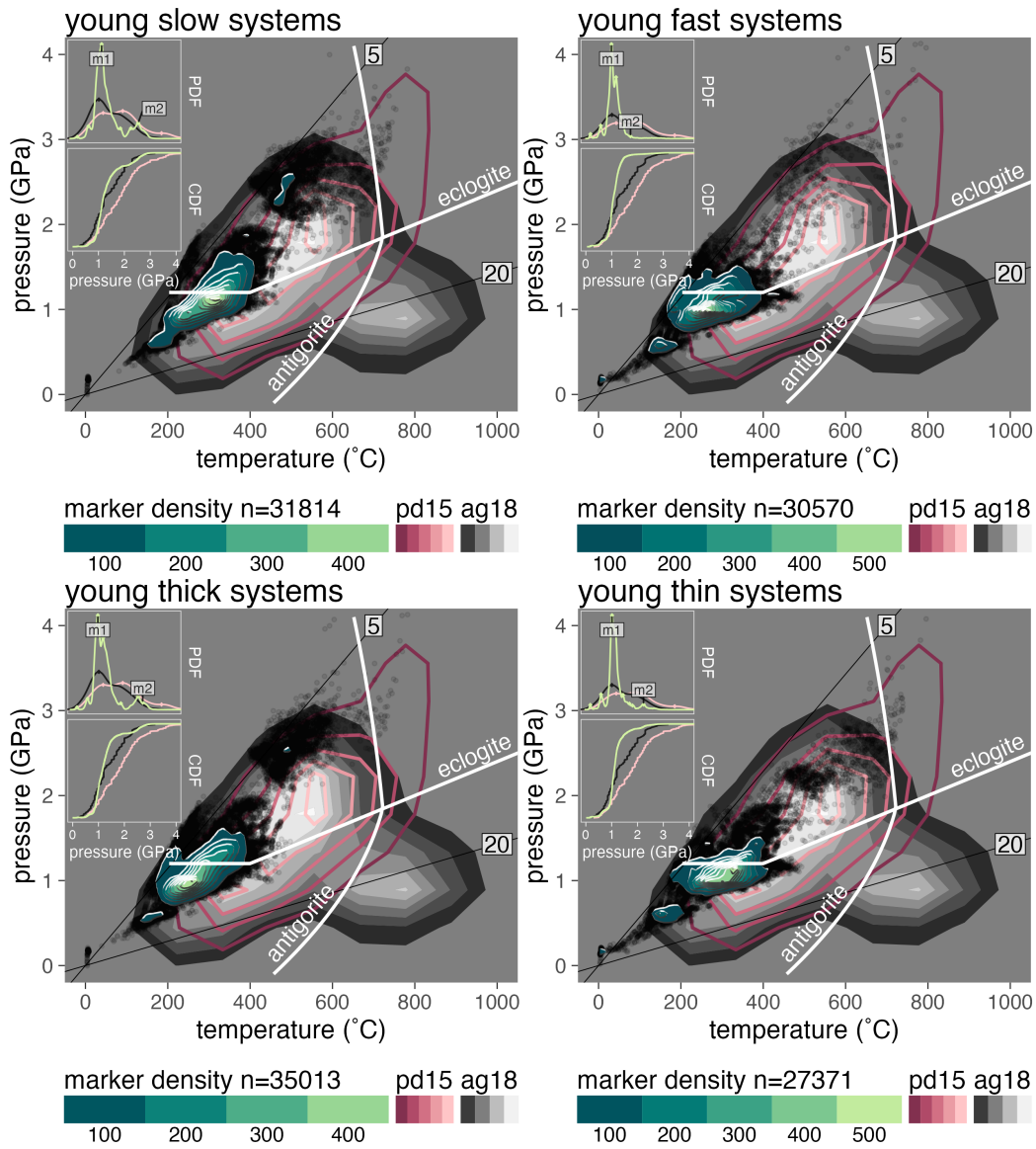


Figure 5: Recovered markers from numerical experiments with young oceanic plates (32.6-55 Ma). PT diagrams showing the densities of recovered markers (black points cloud and green Tanaka contours) in comparison with the pd15 (solid red density contours) and ag18 (filled gray density contours) datasets, grouped by thermo-kinematic boundary conditions (16 experiments per plot; boundary conditions summarized in Kerswell et al., 2021). (insets) Probability distribution (top inset) and CDF diagrams with respect to P. Thin lines are thermal gradients labeled in $^{\circ}\text{C}/\text{km}$. Reaction boundaries for eclogitization of oceanic crust and antigorite dehydration are from Ito & Kennedy (1971) and Schmidt & Poli (1998), respectively.

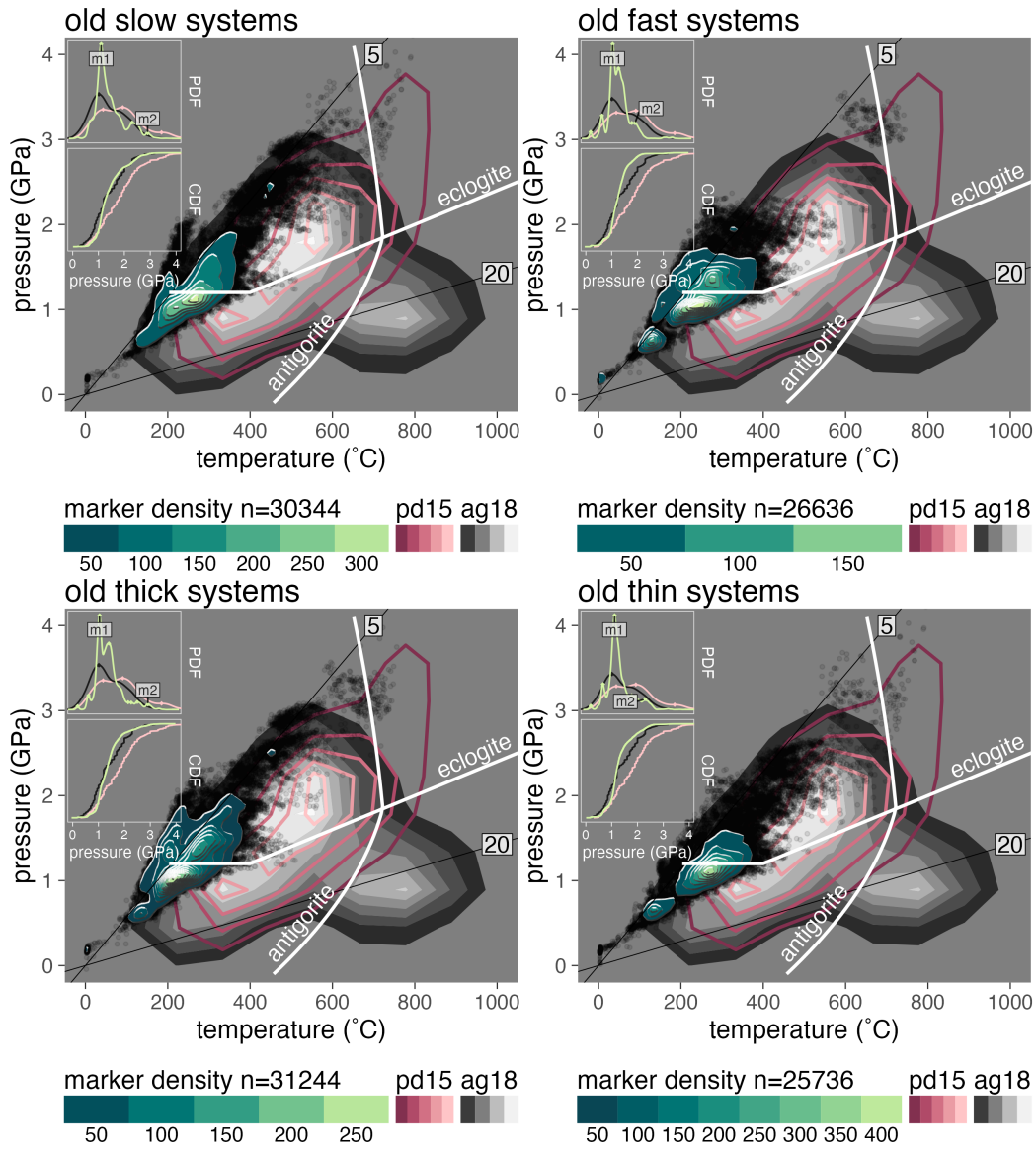


Figure 6: Recovered markers from numerical experiments with older oceanic plates (85–110 Ma). PT diagrams showing the densities of recovered markers (black points cloud and green Tanaka contours) in comparison with the pd15 (solid red density contours) and ag18 (filled gray density contours) datasets, grouped by thermo-kinematic boundary conditions (16 experiments per plot; boundary conditions summarized in Kerswell et al., 2021). (insets) Probability distribution (top inset) and CDF diagrams with respect to P. Thin lines are thermal gradients labeled in °C/km. Reaction boundaries for eclogitization of oceanic crust and antigorite dehydration are from Ito & Kennedy (1971) and Schmidt & Poli (1998), respectively.

371 correlate with oceanic plate age. Although oceanic plate age strongly affects the aver-
 372 age PT gradients of recovered material, it does not strongly shift marker recovery up or
 373 down the subduction interface.

374 **3.2.2 Convergence Velocity Effect**

375 P's and T's of recovered markers respond strongly to changes in convergence ve-
 376 locity (Figure 7, Table 1). Both P modes are strongly inversely correlated with conver-
 377 gence velocity, showing a mean increase from 1.09 ± 0.03 GPa (P mode1) and $1.91 \pm$
 378 0.33 GPa (P mode2) for fast moving plates (100 km/Ma) to about 1.37 ± 0.06 GPa (P
 379 mode1) and 2.64 ± 0.08 GPa (P mode2) for slow moving plates (40 km/Ma). However,
 380 the dominant P mode (P mode1) does not change significantly until convergence veloc-
 381 ity drops below 66 km/Ma (Table 1). Both T modes are strongly inversely correlated
 382 with convergence velocity, showing a mean increase from 249.3 ± 6.6 °C (T mode1) and
 383 371.8 ± 60.8 °C (T mode2) for fast moving plates (100 km/Ma) to about 311.6 ± 1.5
 384 °C (T mode1) and 542.5 ± 74.3 °C (T mode2) for slow moving plates (40 km/Ma). Nei-
 385 ther PT gradient modes, nor recovery rate correlate with convergence velocity. In sum-
 386 mary, decreasing convergence velocity shifts marker recovery to warmer and deeper con-
 387 ditions along the subduction interface without significantly changing the average ther-
 388 mal gradient of subducted material.

389 **3.2.3 Upper-plate Thickness Effect**

390 From the same numerical experiments used to trace markers, an association be-
 391 tween upper-plate thickness and mechanical coupling depths was demonstrated (Kerswell
 392 et al., 2021). P distributions of markers were thus expected to respond strongly to changes
 393 in upper-plate thickness. However, a surprisingly negligible effect was observed (Figure
 394 7). For example, neither of the P modes, nor T mode2 (usually the most deeply subducted
 395 markers) correlate with upper-plate thickness. In contrast, both PT gradient modes and
 396 the dominant T mode (T mode1) inversely correlate with upper-plate thickness. Recov-
 397 ery rate is correlated with upper-plate thickness and not with any other boundary con-
 398 dition, indicating higher recovery rates are more likely underneath thick upper-plates.
 399 Recovery rates show a mean decrease from 10.65 ± 0.32 % for thicker plates (≥ 78 km-
 400 thick) to 8.09 ± 0.3 % for thinner upper-plates (≤ 62 km-thick). In summary, thin upper-

401 plates are more likely to produce warmer thermal gradients, higher T's, and lower re-
 402 covery rates.

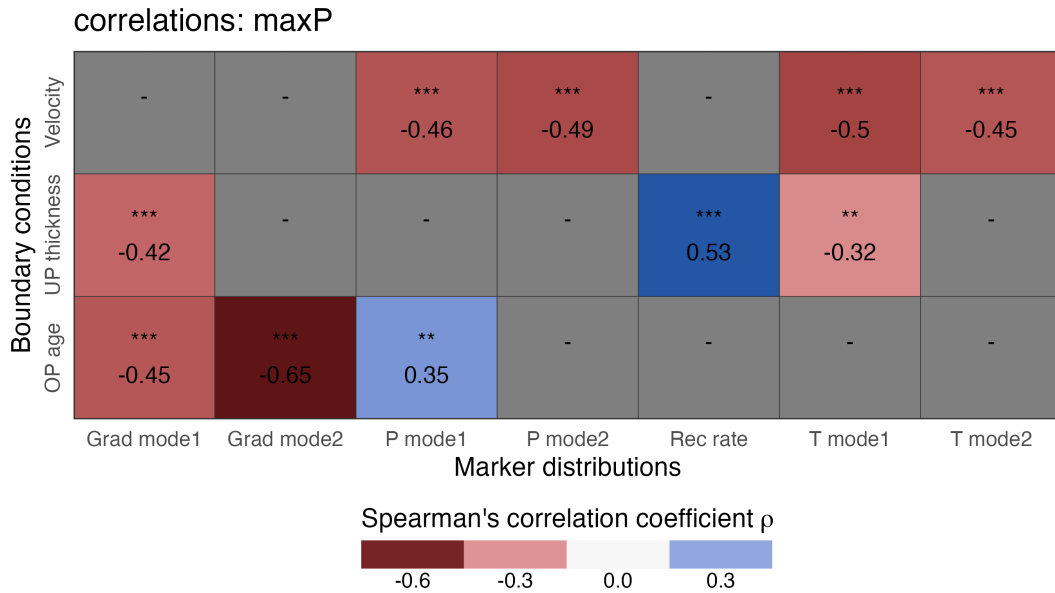


Figure 7: Correlations among marker recovery modes and thermo-kinematic boundary conditions. The dominant recovery mode (mode1) indicates the position of the tallest density peak with respect to P, T, or thermal gradient (i.e. conditions from which the greatest number of markers are recovered), while mode2 indicates the position of the warmest, deepest, or highest gradient density peak (i.e. conditions from which deeply subducted markers are recovered). While oceanic plate age and upper-plate thickness more strongly affect the average thermal gradients of recovered markers (stronger correlations with gradient modes and T mode1), convergence velocity more strongly affects the depths of recovery along the subduction interface, especially for deeply subducted markers (stronger correlation with P modes and T mode2). The dominant T mode (T mode1) and recovery rate are correlated with upper-plate thickness, but not with any other boundary condition. Symbols indicate the Spearman's rank correlation coefficient that measures the significance of monotonic correlations. *** $\rho \leq 0.001$, ** $\rho \leq 0.01$, * $\rho \leq 0.05$, - $\rho \geq 0.05$.

Table 1: Subduction zone parameters and marker classification summary

Initial Boundary Conditions					Marker Classification Summary							
model	Φ	Z_{UP}	age	\vec{v}	recovered	rec. rate	P model1	P mode2	T model1	T mode2	grad model1	grad mode2
	km	km	Ma	km/Ma		%	GPa	GPa	$^{\circ}\text{C}$	$^{\circ}\text{C}$	$^{\circ}\text{C}/\text{km}$	$^{\circ}\text{C}/\text{km}$
cda46	13.0	46	32.6	40	1482±28	7.8±0.14	1.12±0.00	2.46±0.04	336±2	584±138	8.2±0.02	9.5±0.04
cda62	13.0	62	32.6	40	1351±24	7.2±0.12	1.12±0.00	2.24±0.26	332±2	534±36	8.3±0.02	8.3±0.02
cda78	13.0	78	32.6	40	1863±30	9.9±0.16	1.39±0.00	2.38±0.02	352±2	477±2	5.9±0.02	9.3±1.66
cda94	13.0	94	32.6	40	1932±28	10.2±0.14	1.24±0.00	2.65±0.02	341±2	502±26	5.6±0.02	7.8±0.04
cdb46	21.5	46	32.6	66	1806±34	9.6±0.18	1.04±0.00	2.37±0.74	334±2	657±2	8.3±0.04	8.4±0.38
cdb62	21.5	62	32.6	66	1405±20	7.4±0.10	1±0.00	2.16±0.00	281±2	531±32	7.8±0.04	10±0.06
cdb78	21.5	78	32.6	66	1884±32	10±0.18	0.92±0.00	2.49±0.08	264±2	541±6	8.1±0.04	8.1±0.04
cdb94	21.5	94	32.6	66	2330±124	12.3±0.66	1.16±0.16	2.64±0.12	291±2	464±44	7.5±0.02	7.9±1.10
cdc46	26.1	46	32.6	80	1736±46	9.2±0.24	1.02±0.00	1.27±0.68	320±0	475±162	8.8±0.40	9.1±0.98
cdc62	26.1	62	32.6	80	1288±28	6.8±0.16	0.99±0.00	2.01±0.00	264±2	531±2	6.7±0.02	8.6±0.92
cdc78	26.1	78	32.6	80	1801±24	9.5±0.14	0.94±0.10	2.88±0.16	283±2	519±28	7.8±0.02	8.1±2.00
cdc94	26.1	94	32.6	80	2158±26	11.4±0.14	1.14±0.00	3.01±0.02	274±0	533±2	6.7±0.04	9.8±0.04

Table 1: Subduction zone parameters and marker classification summary (*continued*)

Initial Boundary Conditions					Marker Classification Summary							
model	Φ	Z_{UP}	age	\vec{v}	recovered	rec. rate	P model1	P mode2	T model1	T mode2	grad model1	grad mode2
	km	km	Ma	km/Ma		%	GPa	GPa	$^{\circ}\text{C}$	$^{\circ}\text{C}$	$^{\circ}\text{C}/\text{km}$	$^{\circ}\text{C}/\text{km}$
cdd46	32.6	46	32.6	100	1055±58	5.6±0.30	1±0.00	1.76±0.14	226±0	465±50	5.9±0.02	8.5±0.06
cdd62	32.6	62	32.6	100	1365±28	7.2±0.14	0.99±0.00	1.63±0.16	262±2	342±30	5.6±0.04	8.9±0.04
cdd78	32.6	78	32.6	100	1889±28	10±0.16	1±0.00	1.93±0.08	264±2	512±2	7.5±0.04	11.8±1.56
cdd94	32.6	94	32.6	100	2716±32	14.4±0.16	1.23±0.00	2.9±0.00	242±38	660±6	7.3±0.02	7.3±0.02
cde46	22.0	46	55.0	40	1612±36	8.5±0.18	1.11±0.00	2.83±0.54	315±2	675±90	6.7±0.02	7.9±0.94
cde62	22.0	62	55.0	40	1794±50	9.5±0.26	1.08±0.00	2.24±0.00	285±2	485±2	6.1±0.00	7.4±0.64
cde78	22.0	78	55.0	40	1866±34	9.9±0.18	1.37±0.00	2.52±0.00	315±2	507±98	5.9±0.06	7.5±0.02
cde94	22.0	94	55.0	40	1808±20	9.6±0.10	2.33±0.86	2.54±0.00	319±2	431±0	5±0.02	7.2±0.02
cdf46	36.3	46	55.0	66	2246±56	11.9±0.30	1.11±0.04	2.68±0.28	308±2	673±14	7.6±0.02	7.6±0.02
cdf62	36.3	62	55.0	66	1569±38	8.3±0.20	1.14±0.00	2.2±0.06	265±2	582±130	6.9±0.02	6.9±0.02
cdf78	36.3	78	55.0	66	1621±26	8.6±0.14	0.99±0.00	2.75±0.18	228±2	545±8	7±0.02	7.5±1.16
cdf94	36.3	94	55.0	66	1964±30	10.4±0.16	0.93±0.00	2.79±0.02	216±0	597±212	6.6±0.02	6.6±0.02

Table 1: Subduction zone parameters and marker classification summary (*continued*)

Initial Boundary Conditions					Marker Classification Summary							
model	Φ	Z_{UP}	age	\vec{v}	recovered	rec. rate	P model1	P mode2	T model1	T mode2	grad model1	grad mode2
	km	km	Ma	km/Ma		%	GPa	GPa	$^{\circ}\text{C}$	$^{\circ}\text{C}$	$^{\circ}\text{C}/\text{km}$	$^{\circ}\text{C}/\text{km}$
cdg46	44.0	46	55.0	80	2101±74	11.1±0.40	1.2±0.00	1.96±0.04	338±2	338±2	8.1±0.16	8.2±1.26
cdg62	44.0	62	55.0	80	1334±24	7.1±0.12	1±0.00	1.74±0.06	218±4	277±48	5.2±0.02	7.5±0.04
cdg78	44.0	78	55.0	80	1585±26	8.4±0.14	1.01±0.00	2.21±0.02	238±2	529±210	4.9±0.02	7.1±0.02
cdg94	44.0	94	55.0	80	2132±22	11.3±0.12	0.98±0.00	2.69±0.02	209±0	402±36	6.4±0.02	9.4±0.10
cdh46	55.0	46	55.0	100	947±16	5±0.08	0.95±0.00	1.63±0.26	273±4	368±98	7±0.18	9.2±0.48
cdh62	55.0	62	55.0	100	1448±24	7.7±0.12	0.99±0.00	1.73±0.00	237±36	243±2	6.9±1.46	7.1±0.02
cdh78	55.0	78	55.0	100	1631±22	8.6±0.12	0.99±0.02	1.59±0.26	215±10	256±84	6.6±1.36	6.8±0.16
cdh94	55.0	94	55.0	100	2281±28	12.1±0.14	0.88±0.00	1.24±0.14	203±0	275±2	6.7±0.02	10.3±0.62
cdi46	34.0	46	85.0	40	1275±24	6.8±0.14	1.17±0.00	3.55±0.32	287±2	721±72	6.6±0.02	6.6±0.02
cdi62	34.0	62	85.0	40	1915±34	10.1±0.18	1.09±0.00	2.28±0.00	257±2	494±286	5.6±0.76	6.7±0.04
cdi78	34.0	78	85.0	40	2043±24	10.8±0.12	1.65±0.02	2.56±0.00	320±2	443±4	5.4±0.02	6.5±0.02
cdi94	34.0	94	85.0	40	2007±38	10.6±0.20	1.66±0.02	2.94±0.00	292±2	493±6	5.1±0.02	6.4±0.02

Table 1: Subduction zone parameters and marker classification summary (*continued*)

Initial Boundary Conditions					Marker Classification Summary							
model	Φ	Z_{UP}	age	\vec{v}	recovered	rec. rate	P model1	P mode2	T model1	T mode2	grad model1	grad mode2
	km	km	Ma	km/Ma		%	GPa	GPa	$^{\circ}\text{C}$	$^{\circ}\text{C}$	$^{\circ}\text{C}/\text{km}$	$^{\circ}\text{C}/\text{km}$
cdj46	56.1	46	85.0	66	1656 \pm 100	8.8 \pm 0.52	1.07 \pm 0.00	2.55 \pm 0.58	273 \pm 2	616 \pm 318	6.4 \pm 0.06	7.4 \pm 0.12
cdj62	56.1	62	85.0	66	1364 \pm 28	7.2 \pm 0.14	1.09 \pm 0.00	2.13 \pm 0.04	238 \pm 2	516 \pm 24	6.3 \pm 0.02	6.3 \pm 0.02
cdj78	56.1	78	85.0	66	1326 \pm 28	7 \pm 0.14	1.22 \pm 0.00	1.97 \pm 0.02	202 \pm 0	315 \pm 0	4.5 \pm 0.02	6.5 \pm 0.06
cdj94	56.1	94	85.0	66	1849 \pm 26	9.8 \pm 0.14	1.03 \pm 0.00	1.52 \pm 0.00	206 \pm 0	206 \pm 0	5.9 \pm 0.02	5.9 \pm 0.02
cdk46	68.0	46	85.0	80	1463 \pm 24	7.8 \pm 0.14	1.06 \pm 0.02	1.11 \pm 0.26	270 \pm 2	400 \pm 120	7.5 \pm 0.02	7.5 \pm 0.02
cdk62	68.0	62	85.0	80	1204 \pm 20	6.4 \pm 0.10	1.07 \pm 0.00	1.83 \pm 0.00	220 \pm 2	452 \pm 170	4.7 \pm 0.02	6.7 \pm 0.04
cdk78	68.0	78	85.0	80	1540 \pm 36	8.2 \pm 0.20	1.02 \pm 0.04	1.78 \pm 0.34	214 \pm 8	214 \pm 8	6 \pm 1.58	6.9 \pm 0.90
cdk94	68.0	94	85.0	80	2032 \pm 32	10.8 \pm 0.16	1.04 \pm 0.00	3.19 \pm 0.06	265 \pm 2	677 \pm 30	6 \pm 0.02	6 \pm 0.02
cdl46	85.0	46	85.0	100	714 \pm 16	3.8 \pm 0.08	1.1 \pm 0.00	1.56 \pm 0.02	268 \pm 2	268 \pm 2	6 \pm 0.06	6.5 \pm 2.78
cdl62	85.0	62	85.0	100	1096 \pm 22	5.8 \pm 0.12	1.02 \pm 0.00	2.23 \pm 0.02	246 \pm 2	466 \pm 126	6.8 \pm 0.18	6.8 \pm 0.18
cdl78	85.0	78	85.0	100	1663 \pm 42	8.8 \pm 0.22	1.08 \pm 0.18	1.94 \pm 0.02	273 \pm 2	273 \pm 2	4 \pm 0.02	8.9 \pm 2.46
cdl94	85.0	94	85.0	100	1508 \pm 218	8 \pm 1.16	1.23 \pm 0.16	1.27 \pm 0.08	225 \pm 4	370 \pm 70	5.8 \pm 0.06	7.4 \pm 2.74

Table 1: Subduction zone parameters and marker classification summary (*continued*)

Initial Boundary Conditions					Marker Classification Summary							
model	Φ	Z_{UP}	age	\vec{v}	recovered	rec. rate	P model1	P mode2	T model1	T mode2	grad model1	grad mode2
	km	km	Ma	km/Ma		%	GPa	GPa	$^{\circ}\text{C}$	$^{\circ}\text{C}$	$^{\circ}\text{C}/\text{km}$	$^{\circ}\text{C}/\text{km}$
cdm46	44.0	46	110.0	40	1390 \pm 24	7.4 \pm 0.12	1.39 \pm 0.00	3.14 \pm 0.02	320 \pm 2	711 \pm 6	6.1 \pm 0.02	8.1 \pm 1.94
cdm62	44.0	62	110.0	40	2326 \pm 28	12.3 \pm 0.14	1.21 \pm 0.00	2.45 \pm 0.00	281 \pm 0	439 \pm 2	5.5 \pm 0.38	5.7 \pm 0.04
cdm78	44.0	78	110.0	40	1828 \pm 36	9.7 \pm 0.18	1.48 \pm 0.00	2.51 \pm 0.00	331 \pm 4	668 \pm 208	5.5 \pm 0.02	6.4 \pm 1.04
cdm94	44.0	94	110.0	40	1901 \pm 28	10.1 \pm 0.14	1.53 \pm 0.00	2.87 \pm 0.00	302 \pm 2	517 \pm 210	5.3 \pm 0.02	6 \pm 0.02
cdn46	72.6	46	110.0	66	1942 \pm 88	10.3 \pm 0.46	1.25 \pm 0.00	2.3 \pm 0.08	283 \pm 2	637 \pm 70	7.1 \pm 0.06	7.1 \pm 0.06
cdn62	72.6	62	110.0	66	1217 \pm 24	6.5 \pm 0.14	1.13 \pm 0.00	2.15 \pm 0.24	269 \pm 0	559 \pm 136	6.9 \pm 0.06	6.9 \pm 0.06
cdn78	72.6	78	110.0	66	1684 \pm 38	8.9 \pm 0.20	1.38 \pm 0.00	1.38 \pm 0.00	212 \pm 2	429 \pm 4	3.9 \pm 0.02	7 \pm 1.22
cdn94	72.6	94	110.0	66	1685 \pm 26	8.9 \pm 0.14	1.06 \pm 0.00	1.77 \pm 0.36	203 \pm 2	299 \pm 144	5.6 \pm 0.04	6.6 \pm 0.44
cdo46	88.0	46	110.0	80	1476 \pm 128	7.8 \pm 0.68	1.21 \pm 0.04	1.75 \pm 0.86	280 \pm 2	343 \pm 74	7.4 \pm 0.08	7.4 \pm 0.08
cdo62	88.0	62	110.0	80	1328 \pm 82	7.1 \pm 0.44	1.06 \pm 0.02	2.31 \pm 0.60	252 \pm 4	577 \pm 230	7.1 \pm 0.08	7.1 \pm 0.08
cdo78	88.0	78	110.0	80	1629 \pm 34	8.7 \pm 0.18	0.92 \pm 0.00	1.38 \pm 0.02	194 \pm 2	376 \pm 90	4.1 \pm 0.02	6.9 \pm 1.58
cdo94	88.0	94	110.0	80	1997 \pm 152	10.6 \pm 0.80	1.07 \pm 0.22	2.68 \pm 1.86	252 \pm 26	526 \pm 410	5.7 \pm 0.02	6.9 \pm 2.58

Table 1: Subduction zone parameters and marker classification summary (*continued*)

Initial Boundary Conditions					Marker Classification Summary							
model	Φ	Z_{UP}	age	\vec{v}	recovered	rec. rate	P model1	P mode2	T model1	T mode2	grad model1	grad mode2
	km	km	Ma	km/Ma		%	GPa	GPa	$^{\circ}\text{C}$	$^{\circ}\text{C}$	$^{\circ}\text{C}/\text{km}$	$^{\circ}\text{C}/\text{km}$
cdp46	110.0	46	110.0	100	1518 \pm 144	8 \pm 0.76	1.27 \pm 0.00	2.15 \pm 3.24	301 \pm 2	306 \pm 30	7 \pm 0.06	7 \pm 0.06
cdp62	110.0	62	110.0	100	1371 \pm 114	7.3 \pm 0.60	1.12 \pm 0.00	2.06 \pm 0.00	234 \pm 2	346 \pm 312	5.2 \pm 0.78	9.6 \pm 1.62
cdp78	110.0	78	110.0	100	1650 \pm 36	8.8 \pm 0.20	1.11 \pm 0.00	1.82 \pm 0.24	274 \pm 2	541 \pm 70	6.1 \pm 1.08	6.3 \pm 0.06
cdp94	110.0	94	110.0	100	1848 \pm 156	9.8 \pm 0.84	1.41 \pm 0.12	3.17 \pm 0.66	244 \pm 0	259 \pm 90	5.7 \pm 0.02	5.7 \pm 0.02

Classifier uncertainties (2σ) estimated by running the classifier 30 times with random marker samples (jackknife sample proportion: 90%)

4 Discussion

4.1 Thermo-Kinematic Controls on Rock Recovery

While the combined distribution of markers recovered from all numerical experiments shows appreciable deviations from PT estimates compiled by Penniston-Dorland et al. (2015) and Agard et al. (2018), markers recovered from simulations with the youngest oceanic plates (32.6-55 Ma) and the slowest convergence velocities (40-66 km/Ma) begin to resemble the distribution of exhumed HP rocks (compare Figure 4 with Figures 5 & 6) with respect to thermal gradients and P distributions. Slower subduction of younger plates increases marker thermal gradients and strongly shifts marker recovery down the subduction interface (strong correlations with Grad mode1 and P mode1 & mode2, Figure 7). The correlations in Figure 7 also suggest a shift towards warmer recovery conditions should be complemented by thin upper-plates—implying systems with thin upper-plates, slow convergence, and young oceanic plates should be most consistent with the distribution of rock recovery implied by pd15 and ag18 (Figure 5). This correspondence might appear consistent with inferences that the rock record is composed primarily of rock bodies exhumed from “warm” subduction settings (Abers et al., 2017; van Keken et al., 2018). However, our numerical experiments also show that recovery rates do not correlate with oceanic plate age or convergence velocity, and that recovery rates are poorer for thinner upper-plates (Figure 7). Correlations between thermo-kinematic boundary conditions and recovery rates drawn from many tens of thousands of recovered markers across numerous simulations counter the notion that preferential recovery is happening in “warm” subduction settings.

Besides recovery rates of subducting markers, other dynamic characteristics appear to correlate with oceanic plate age and convergence velocity. For example, simulations with slow convergence velocities (e.g. models: cda, cde, cdi, cdm) tend to have higher subduction angles (see Supplementary ??) with thicker subduction interfaces that allow more markers to subduct to deeper, and thus warmer, conditions compared to other experiments (e.g. models: cdd, cdh, cdl, cdp) that form narrow interfaces with shallow choke points (e.g. see Supplementary ??). Observationally, the angle of subduction does not correlate significantly with oceanic plate age or convergence velocity, but rather inversely with the duration of subduction (Hu & Gurnis, 2020). Thus, the rock record might indicate preferential exhumation during the earlier stages of subduction when subduction

435 angles were steeper (although not necessarily during subduction initiation), even for older
436 oceanic plates. More generally, differences in plate flexibility, overall subduction geom-
437 etry, and velocity of plate motions strongly affect PT distributions of rock recovery (Monie
438 & Agard, 2009)—rather than strictly “warm” versus “cool” subduction settings *per se*.
439 In other words, thermo-kinematic boundary conditions typically inferred to strictly reg-
440 ulate *thermal* effects (e.g. young-slow oceanic plates supporting warmer thermal gradi-
441 ents) may indeed be regulating more *dynamic* effects (e.g. young-slow oceanic plates flex-
442 ibly rolling back to support deeper subduction of material along thicker interfaces) that
443 are subsequently *observed* as thermal effects (average increase in marker PT’s).

444 4.2 Comparison with other Numerical Experiments

445 Marker PT distributions and their correlations with thermo-kinematic boundary
446 conditions presented above are determined directly from large samples of recovered ma-
447 terial evolving dynamically in a deforming subduction interface (analogous to reconstruct-
448 ing thermal gradients from large random samples of exhumed HP rocks). In contrast,
449 other studies investigating thermal responses to variable boundary conditions typically
450 determine PT gradients statically along discrete surfaces representing megathrust faults
451 (e.g. Abers et al., 2006; Currie et al., 2004; Davies, 1999; Furukawa, 1993; Gao & Wang,
452 2014; McKenzie, 1969; Molnar & England, 1990; Peacock & Wang, 1999; Syracuse et al.,
453 2010; van Keken et al., 2011, 2019; Wada & Wang, 2009) or dynamically by “finding”
454 the subduction interface heuristically at each timestep (e.g. Arcay, 2017; Holt & Con-
455 dit, 2021; Ruh et al., 2015). Other studies using similar geodynamic codes have traced
456 many fewer markers (typically dozens vs. $\sim 120,000$; Faccenda et al., 2008; Gerya et al.,
457 2002; Sizova et al., 2010; Yamato et al., 2007, 2008) from a narrower range of thermo-
458 kinematic boundary conditions, so they implicitly have less statistical rigor. This study
459 stresses the importance of large sample sizes because individual marker PT paths can
460 vary considerably within a single simulation, yet important modes of recovery become
461 apparent from density peaks as more markers are traced. Furthermore, most other stud-
462 ies make no attempt to determine peak PT conditions related to detachment and *recov-*
463 *ery* (with some exceptions, e.g. Roda et al., 2012, 2020), so marker PT paths are less
464 analogous to PT paths determined by applying petrologic modeling.

4.3 Comparison with Geophysical Observations

The locations of important recovery modes determined from numerical experiments correspond closely with the depths of important mechanical transitions inferred from seismic imaging studies and surface heat flow observations. For example, the dominant recovery mode common among all numerical experiments at about 1 GPa (Table 1 & Figure 4) is consistent with a layer of low seismic velocities and high V_p/V_s ratios observed at numerous subduction zones between 20-50 km depth (Bostock, 2013). While considerable unknowns persist about the nature of deformation in this region (Bostock, 2013; Tewksbury-Christle & Behr, 2021), the low-velocity zone, accompanied by low-frequency and slow-slip seismic events, is often interpreted as a transitional brittle-ductile shear zone actively accommodating underplating of subducted material and/or formation of a tectonic *mélange* around the base of the continental Moho (Audet & Kim, 2016; Audet & Schaeffer, 2018; Bostock, 2013; Calvert et al., 2011, 2020; Delph et al., 2021).

Formation of low-velocity zones and their geophysical properties are generally attributed to high pore-fluid pressures caused by metamorphic reactions relating to the dehydration of oceanic crust (Hacker, 2008; Rondenay et al., 2008; van Keken et al., 2011). Surprisingly, despite our numerical implementation of a relatively simple model for dehydration of oceanic crust (Ito & Kennedy, 1971; Kerswell et al., 2021), and a relatively simple visco-plastic rheological model (Gerya & Yuen, 2003; Kerswell et al., 2021), the primary mode of marker recovery at 1.15 ± 0.46 GPa (2σ , Table 1) coincides closely with the expected region for shallow underplating according to geophysical constraints (35 ± 15 km or 1.0 ± 0.4 GPa). The size of the markers dataset ($n = 119,364$ recovered markers) and prevalence of marker recovery from 1 GPa suggest that although dehydration may indeed trigger detachment of subducting rocks, other factors—notably the compositional and mechanical transition in the upper-plate across the Moho—also influence detachment at this depth.

The termination of the low-velocity zone at depths beyond the continental Moho marks another important mechanical transition. This second transition is often interpreted as the onset of mechanical plate coupling near 80 km (or 2.3 GPa) and coincides well with the deeper recovery modes determined from recovered markers at 2.2 ± 1.1 GPa (2σ , Table 1). Between these two modes of recovery at ~ 40 and ~ 80 km lies a gap that

496 coincides with the highest sample density of exhumed HP rocks compiled in pd15 and
497 ag18 (Figure 4). This recovery gap is discussed in the following section.

498 **4.4 The Marker Recovery Gap**

499 Although recovered markers partially overlap with the range of PT estimates com-
500 piled in the pd15 and ag18 datasets, the differences between distributions of recovered
501 markers and natural samples are numerous, including: (1) an obvious lack of markers
502 recovered from ≥ 15 °C/km (0.002%) compared to pd15 and ag18 (37-48%, Figure 4),
503 (2) recovery of markers from a single dominant mode near 1 GPa and 300 °C compared
504 to more broadly distributed multimodal recovery across PT space for natural samples
505 (Figure 4), (3) a general shift towards lower T's and cooler thermal gradients for mark-
506 ers compared to natural samples, and (4) a remarkable gap in marker recovery near 2
507 GPa and 550 °C that coincides with the highest density of natural samples (Figure 4).
508 In fact, across 64 numerical experiments with wide-ranging initial conditions less than
509 1% (0.63%) of markers are recovered from between 1.8-2.2 GPa and 475-625 °C. Why
510 might this gap occur? Four possibilities are considered:

- 511 1. Simple rheological models preclude certain recovery mechanisms (poor implemen-
512 tation of subduction interface mechanics, i.e., modeling uncertainty, Section 4.3)
- 513 2. Peak metamorphic conditions are systematically misinterpreted (peak metamor-
514 phic conditions do not correspond to maxP or PT paths are not well constrained,
515 i.e., petrologic uncertainties, e.g., see Penniston-Dorland et al., 2015)
- 516 3. Rocks are frequently (re)sampled from the same peak metamorphic conditions and
517 other rocks from different metamorphic grades are infrequently sampled (selective
518 nonrandom sampling, i.e., scientific bias, e.g., see Agard et al., 2018)
- 519 4. Rocks are recovered during short-lived events (e.g., subduction of seamounts, Agard
520 et al., 2009) that are not implemented in our numerical experiments, rather than
521 recovered during steady-state subduction within a serpentine-rich tectonic mélange
522 that is characteristic of our numerical experiments (i.e., geodynamic uncertain-
523 ties)

524 **4.4.1 Numerical Modeling Uncertainties**

525 Simplifying assumptions in our numerical experiments influence thermal gradients
526 and dynamics of rock recovery from the subducting oceanic plate. Substantially lower
527 T's and thermal gradients in numerical experiments compared to natural samples (Fig-
528 ure 4) might indicate imperfect implementation of heat generation and transfer (Kohn
529 et al., 2018; Penniston-Dorland et al., 2015). Our hydrologic model and implementation
530 of serpentine rheology in the numerical experiments creates a weak interface. A stronger
531 rheology (e.g., quartz or a mixed melange zone Beall et al., 2019; Ioannidi et al., 2021),
532 or a stronger serpentine flow law (Burdette & Hirth, 2022), would yield greater heating
533 and higher T's from enhanced viscous dissipation along the subduction interface (Kohn
534 et al., 2018). In principle, a stronger rheology might shift the overall PT distribution of
535 markers to higher T's and help fill in the marker recovery gap around 2 GPa and 550
536 °C, and/or possibly change flow to extract rocks more broadly along the subduction in-
537 terface. Although the effects of different interface rheologies on thermal structure or rock
538 recovery were not explicitly explored in this study, even numerical simulations with the
539 smallest PT discrepancies between markers and natural samples (youngest oceanic plates
540 and slowest convergence velocities, Figures 5 & 6) exhibit the same sizeable gap in marker
541 recovery around 2 GPa and 550 °C. Thus, higher T's alone would not seem to close the
542 gap.

543 **4.4.2 Petrologic Uncertainties**

544 Interpreting peak metamorphic conditions of complex polymetamorphic rocks is
545 challenging with many sources of uncertainties. However, a global shift in PT estimates
546 of natural samples towards warmer conditions compared to recovered markers would im-
547 ply that decades of field observations, conventional thermobarometry (e.g. Spear & Selver-
548 stone, 1983), phase equilibria modeling (e.g. Connolly, 2005), trace element thermom-
549 etry (e.g. Ferry & Watson, 2007; Kohn, 2020), and Raman Spectroscopy of Carbona-
550 ceous Material thermometry (Beyssac et al., 2002) from many independent localities world-
551 wide (e.g. Agard et al., 2009, 2018; Angiboust et al., 2009, 2012a, 2016; Avigad & Gar-
552 funkel, 1991; Monie & Agard, 2009; Plunder et al., 2013, 2015) have systematically mis-
553 interpreted the prograde and retrograde histories of exhumed HP rocks. The consistency
554 of independent analytical techniques suggests systematic bias is unlikely and estimated

555 uncertainties are generally too small for this argument to be viable (Penniston-Dorland
556 et al., 2015).

557 ***4.4.3 Selective Sampling and Scientific Bias***

558 At least two factors might lead to scientific bias. First, the application of conven-
559 tional thermobarometry is easier for certain rock types and mineral assemblages (e.g. eclogite-
560 facies metabasites and metapelitic schists) than for others (e.g. quartzites, metagraywackes).
561 Second, certain subduction complexes expose more rocks than others. These factors lead
562 to sampling bias, both in the rocks that are selected for analysis and which subduction
563 complexes contribute most to compilations. For example, a PT condition of ~ 2 GPa
564 and 550 °C typically yields assemblages that are both recognizable in the field (eclog-
565 ites, *sensu stricto*, and kyanite- or chloritoid-schists) and amenable to thermobaromet-
566 ric calculations and petrologic modeling. This fact may lead to oversampling of the rocks
567 that yield these PT conditions and the subduction zones that expose these rocks. In Penniston-
568 Dorland et al. (2015), the western and central European Alps, which contain many rocks
569 that equilibrated near this PT condition, represented ~ 90 samples across < 1000 km
570 (~ 1 sample per 100 km), whereas the Himalaya and Andes, which contained more di-
571 verse PT conditions, represented only ~ 1 sample per 300-400 km. Some subduction zones
572 are not represented at all in these datasets (e.g. central and western Aleutians, Kamchatka,
573 Izu-Bonin-Marianas, Philippines, Indonesia, etc.), either because metamorphic rocks are
574 not exposed or rock types are not amenable to petrologic investigation. Correcting for
575 this type of bias is challenging because it would require large random samples of exhumed
576 HP rocks from localities worldwide and development of new techniques for quantifying
577 PT conditions in diverse rock types.

578 ***4.4.4 Short-lived Events and Geodynamic Uncertainties***

579 Detachment of rocks from the subducting slab might not occur randomly, but rather
580 in response to specific events, such as subduction of asperities or seamounts (e.g. Agard
581 et al., 2009) or abrupt fluid events. Yet no numerical models have attempted to model
582 these events. In the case of seamounts, high surface roughness correlates with higher co-
583 efficients of friction (Gao & Wang, 2014). Higher friction increases heating and T's, driv-
584 ing subduction interface thermal gradients into the field of PT conditions defined by the
585 pd15 and ag18 datasets (Kohn et al., 2018). If asperities become mechanically unsta-

586 ble at depths of $\sim 50\text{-}70$ km, preferential detachment would create an “overabundance”
587 of recorded PT conditions at moderate T (~ 550 °C) at ~ 2 GPa, as observed.

588 Alternatively, although fluid release is modeled in our numerical experiments as con-
589 tinuous, it may occur sporadically. Two dehydration reactions along the subduction in-
590 terface are particularly relevant: the transformation of lawsonite to epidote, and the trans-
591 formation of chlorite (plus quartz) to garnet. Although dehydration of lawsonite is nearly
592 discontinuous in PT space, few rocks show clear evidence for lawsonite immediately prior
593 to peak metamorphism (although such evidence can be subtle). In the context of equi-
594 librium thermodynamics, chlorite dehydration should occur continuously below depths
595 of ~ 35 km, consistent with assumptions of many numerical geodynamic models. How-
596 ever, research suggests substantial overstepping of this reaction, resulting in the abrupt
597 formation of abundant garnet and release of water (Castro & Spear, 2017). Direct geochronol-
598 ogy of garnet growth rates in subduction complexes also suggests abrupt growth and wa-
599 ter release (Dragovic et al., 2015). Because fluids are thought to help trigger brittle fail-
600 ure (earthquakes) that could detach rocks from the subducting slab surface, abrupt re-
601 lease at a depth of $\sim 50\text{-}70$ km might again result in an “overabundance” of recorded
602 PT conditions at P’s of ~ 2 GPa. This mechanism would require relatively consistent
603 degrees of overstepping in rocks of similar bulk composition and would not directly ex-
604 plain higher T’s, however.

605 **5 Conclusion**

606 This study traces PT paths of more than one million markers from 64 subduction
607 simulations representing a large range of presently active subduction zones worldwide.
608 Marker recovery is identified by implementing a “soft” clustering algorithm, and PT dis-
609 tributions of recovered markers are compared among models and with the rock record.
610 Such a large dataset presents a statistically-robust portrait of important recovery modes
611 (where most markers are detached) along the subduction interface. The three most im-
612 portant findings are as follows:

- 613 1. Numerical simulations with relatively simple (de)hydration models and visco-plastic
614 interface rheologies simulate important recovery mechanisms near the base of the
615 continental Moho around 1 GPa and 300 °C (underplating and/or formation of

- 616 tectonic mélanges) and near the depth of mechanical plate coupling around 2.5
617 GPa and 525 °C.
- 618 2. Subduction systems with young oceanic plates, slow convergence velocities, and
619 thin upper-plate lithospheres are most consistent with the rock record, but it is
620 unclear to what extent kinematic effects (young flexible oceanic plates with high
621 subduction angles accommodating deeper subduction of material) rather than ther-
622 mal effects (young oceanic plates supporting higher thermal gradients) drive changes
623 in marker PT distributions. Comparing young-slow-thin numerical experiments
624 to the rock record is not straightforward, however, because recovery rates do not
625 correlate with either oceanic plate age or convergence velocity, and warmer sub-
626 duction zones yield poorer recovery rates.
- 627 3. A gap in marker recovery near 2 GPa and 550 °C coinciding with the highest den-
628 sities of natural samples suggests an “overabundance” of samples are studied from
629 this PT region. Explanations for this “overabundance” might include selective sam-
630 pling of rocks amenable to petrologic investigation (scientific bias), reaction over-
631 stepping (abrupt release of water triggering detachment of rock near 2 GPa and
632 550 °C), or processes such as subduction of seamounts that are not included in
633 numerical simulations. Future work investigating natural samples from a larger
634 range of peak PT conditions and analyzing marker recovery from numerical geo-
635 dynamic models that include new hydrologic models and interface rheologies might
636 help resolve this discrepancy.

637 **Open Research**

638 All data, code, and relevant information for reproducing this work can be found
639 at https://github.com/buchanankerswell/kerswell_et_al_marx, and at <https://doi.org/10.17605/OSF.IO/3EMWF>, the official Open Science Framework data repository.
640 All code is MIT Licensed and free for use and distribution (see license details).
641

642 **Acknowledgments**

643 We gratefully acknowledge high-performance computing support from the Borah
644 compute cluster (DOI: 10.18122/oit/3/boisestate) provided by Boise State Univer-
645 sity’s Research Computing Department. This work was supported by the National Sci-

646 ence Foundation grant OIA1545903 to M. Kohn, S. Penniston-Dorland, and M. Feine-
647 man.

648 References

649 Abers, G., Keken, P. van, Kneller, E., Ferris, A., & Stachnik, J. (2006). The thermal struc-
650 ture of subduction zones constrained by seismic imaging: Implications for slab de-
651 hydration and wedge flow. *Earth and Planetary Science Letters*, *241*(3-4), 387–397.

652 Abers, G., van Keken, P., & Hacker, B. (2017). The cold and relatively dry nature of man-
653 tle forearcs in subduction zones. *Nature Geoscience*, *10*(5), 333–337.

654 Abers, G., Keken, P. van, & Wilson, C. (2020). Deep decoupling in subduction zones:
655 Observations and temperature limits. *Geosphere*, *16*(6), 1408–1424.

656 Agard, P. (2021). Subduction of oceanic lithosphere in the alps: Selective and archety-
657 pal from (slow-spreading) oceans. *Earth-Science Reviews*, *214*, 103517.

658 Agard, P., Yamato, P., Jolivet, L., & Burov, E. (2009). Exhumation of oceanic blueschists
659 and eclogites in subduction zones: Timing and mechanisms. *Earth-Science Reviews*,
660 *92*(1-2), 53–79.

661 Agard, P., Yamato, P., Soret, M., Prigent, C., Guillot, S., Plunder, A., et al. (2016). Plate
662 interface rheological switches during subduction infancy: Control on slab penetra-
663 tion and metamorphic sole formation. *Earth and Planetary Science Letters*, *451*, 208–
664 220.

665 Agard, P., Plunder, A., Angiboust, S., Bonnet, G., & Ruh, J. (2018). The subduction
666 plate interface: Rock record and mechanical coupling (from long to short time scales).
667 *Lithos*, *320-321*, 537–566.

668 Agard, P., Prigent, C., Soret, M., Dubacq, B., Guillot, S., & Deldicque, D. (2020). Slabiti-
669 zation: Mechanisms controlling subduction development and viscous coupling. *Earth-
670 Science Reviews*, *208*, 103259.

- 671 Angiboust, S., Agard, P., Jolivet, L., & Beyssac, O. (2009). The zermatt-saas ophiolite:
 672 The largest (60-km wide) and deepest (c. 70–80 km) continuous slice of oceanic litho-
 673 sphere detached from a subduction zone? *Terra Nova*, *21*(3), 171–180.
- 674 Angiboust, S., Agard, P., Raimbourg, H., Yamato, P., & Huet, B. (2011). Subduction
 675 interface processes recorded by eclogite-facies shear zones (monviso, w. alps). *Lithos*,
 676 *127*(1-2), 222–238.
- 677 Angiboust, S., Langdon, R., Agard, P., Waters, D., & Chopin, C. (2012a). Eclogitiza-
 678 tion of the monviso ophiolite (w. Alps) and implications on subduction dynamics.
 679 *Journal of Metamorphic Geology*, *30*(1), 37–61.
- 680 Angiboust, S., Wolf, S., Burov, E., Agard, P., & Yamato, P. (2012b). Effect of fluid cir-
 681 culation on subduction interface tectonic processes: Insights from thermo-mechanical
 682 numerical modelling. *Earth and Planetary Science Letters*, *357*, 238–248.
- 683 Angiboust, S., Kirsch, J., Oncken, O., Glodny, J., Monié, P., & Rybacki, E. (2015). Prob-
 684 ing the transition between seismically coupled and decoupled segments along an an-
 685 cient subduction interface. *Geochemistry, Geophysics, Geosystems*, *16*(6), 1905–1922.
- 686 Angiboust, S., Agard, P., Glodny, J., Omrani, J., & Oncken, O. (2016). Zagros blueschists:
 687 Episodic underplating and long-lived cooling of a subduction zone. *Earth and Plan-*
 688 *etary Science Letters*, *443*, 48–58.
- 689 Arcay, D. (2017). Modelling the interplate domain in thermo-mechanical simulations of
 690 subduction: Critical effects of resolution and rheology, and consequences on wet man-
 691 tle melting. *Physics of the Earth and Planetary Interiors*, *269*, 112–132.
- 692 Audet, P., & Kim, Y. (2016). Teleseismic constraints on the geological environment of
 693 deep episodic slow earthquakes in subduction zone forearcs: A review. *Tectonophysics*,
 694 *670*, 1–15.

- 695 Audet, P., & Schaeffer, A. (2018). Fluid pressure and shear zone development over the
 696 locked to slow slip region in cascadia. *Science Advances*, *4*(3), eaar2982.
- 697 Avigad, D., & Garfunkel, Z. (1991). Uplift and exhumation of high-pressure metamor-
 698 phic terrains: The example of the cycladic blueschist belt (aegean sea). *Tectonophysics*,
 699 *188*(3-4), 357–372.
- 700 Banfield, J., & Raftery, A. (1993). Model-based gaussian and non-gaussian clustering.
 701 *Biometrics*, 803–821.
- 702 Barlow, H. (1989). Unsupervised learning. *Neural Computation*, *1*(3), 295–311.
- 703 Batchelor, G. (1953). *The theory of homogeneous turbulence*. Cambridge university press.
- 704 Beall, A., Fagereng, Å., & Ellis, S. (2019). Strength of strained two-phase mixtures: Ap-
 705 plication to rapid creep and stress amplification in subduction zone mélange. *Geo-*
 706 *physical Research Letters*, *46*(1), 169–178.
- 707 Bebout, G. (2007). Metamorphic chemical geodynamics of subduction zones. *Earth and*
 708 *Planetary Science Letters*, *260*(3-4), 373–393.
- 709 Bebout, G., & Barton, M. (2002). Tectonic and metasomatic mixing in a high-t, subduction-
 710 zone mélange—insights into the geochemical evolution of the slab–mantle interface.
 711 *Chemical Geology*, *187*(1-2), 79–106.
- 712 Beyssac, O., Goffé, B., Chopin, C., & Rouzaud, J. (2002). Raman spectra of carbona-
 713 ceous material in metasediments: A new geothermometer. *Journal of Metamorphic*
 714 *Geology*, *20*(9), 859–871.
- 715 Bostock, M. (2013). The moho in subduction zones. *Tectonophysics*, *609*, 547–557.
- 716 Boussinesq, J. (1897). *Théorie de l'écoulement tourbillonnant et tumultueux des liquides*
 717 *dans les lits rectilignes a grande section* (Vol. 1). Gauthier-Villars.

- 718 Burdette, E., & Hirth, G. (2022). Creep rheology of antigorite: Experiments at subduc-
719 tion zone conditions. *Journal of Geophysical Research: Solid Earth*, 127(7), e2022JB024260.
- 720 Burov, E., François, T., Agard, P., Le Pourhiet, L., Meyer, B., Tirel, C., et al. (2014).
721 Rheological and geodynamic controls on the mechanisms of subduction and HP/UHP
722 exhumation of crustal rocks during continental collision: Insights from numerical mod-
723 els. *Tectonophysics*, 631, 212–250.
- 724 Calvert, A., Preston, L., & Farahbod, A. (2011). Sedimentary underplating at the cas-
725 cadia mantle-wedge corner revealed by seismic imaging. *Nature Geoscience*, 4(8), 545–
726 548.
- 727 Calvert, A., Bostock, M., Savard, G., & Unsworth, M. (2020). Cascadia low frequency
728 earthquakes at the base of an overpressured subduction shear zone. *Nature Commu-
729 nications*, 11(1), 1–10.
- 730 Castro, A., & Spear, F. (2017). Reaction overstepping and re-evaluation of peak p–t con-
731 ditions of the blueschist unit sifnos, greece: Implications for the cyclades subduction
732 zone. *International Geology Review*, 59(5-6), 548–562.
- 733 Celeux, G., & Govaert, G. (1995). Gaussian parsimonious clustering models. *Pattern Recog-
734 nition*, 28(5), 781–793.
- 735 Cloos, M., & Shreve, R. (1988). Subduction-channel model of prism accretion, melange
736 formation, sediment subduction, and subduction erosion at convergent plate margins:
737 1. Background and description. *Pure and Applied Geophysics*, 128(3), 455–500.
- 738 Connolly, J. (2005). Computation of phase equilibria by linear programming: A tool for
739 geodynamic modeling and its application to subduction zone decarbonation. *Earth
740 and Planetary Science Letters*, 236(1-2), 524–541.
- 741 Currie, C., & Hyndman, R. (2006). The thermal structure of subduction zone back arcs.
742 *Journal of Geophysical Research: Solid Earth*, 111(B8), 1–22.

- 743 Currie, C., Wang, K., Hyndman, R., & He, J. (2004). The thermal effects of steady-state
744 slab-driven mantle flow above a subducting plate: The cascadia subduction zone and
745 backarc. *Earth and Planetary Science Letters*, 223(1-2), 35–48.
- 746 Davies, J. (1999). Simple analytic model for subduction zone thermal structure. *Geo-*
747 *physical Journal International*, 139(3), 823–828.
- 748 Delph, J., Thomas, A., & Levander, A. (2021). Subcretionary tectonics: Linking vari-
749 ability in the expression of subduction along the cascadia forearc. *Earth and Plan-*
750 *etary Science Letters*, 556, 116724.
- 751 Dempster, A., Laird, N., & Rubin, D. (1977). Maximum likelihood from incomplete data
752 via the EM algorithm. *Journal of the Royal Statistical Society: Series B (Method-*
753 *ological)*, 39(1), 1–22.
- 754 Dragovic, B., Baxter, E., & Caddick, M. (2015). Pulsed dehydration and garnet growth
755 during subduction revealed by zoned garnet geochronology and thermodynamic mod-
756 eling, sifnos, greece. *Earth and Planetary Science Letters*, 413, 111–122.
- 757 England, P., Engdahl, R., & Thatcher, W. (2004). Systematic variation in the depths
758 of slabs beneath arc volcanoes. *Geophysical Journal International*, 156(2), 377–408.
- 759 Faccenda, M., Gerya, T., & Chakraborty, S. (2008). Styles of post-subduction collisional
760 orogeny: Influence of convergence velocity, crustal rheology and radiogenic heat pro-
761 duction. *Lithos*, 103(1-2), 257–287.
- 762 Ferris, A., Abers, G., Christensen, D., & Veenstra, E. (2003). High resolution image of
763 the subducted pacific (?) Plate beneath central alaska, 50–150 km depth. *Earth and*
764 *Planetary Science Letters*, 214(3-4), 575–588.
- 765 Ferry, J., & Watson, E. (2007). New thermodynamic models and revised calibrations for
766 the ti-in-zircon and zr-in-rutile thermometers. *Contributions to Mineralogy and Petrol-*
767 *ogy*, 154(4), 429–437.

- 768 Figueiredo, M., & Jain, A. (2002). Unsupervised learning of finite mixture models. *IEEE*
769 *Transactions on Pattern Analysis and Machine Intelligence*, *24*(3), 381–396.
- 770 Fisher, D., Hooker, J., Smye, A., & Chen, T. (2021). Insights from the geological record
771 of deformation along the subduction interface at depths of seismogenesis. *Geosphere*,
772 *17*(6), 1686–1703.
- 773 Fraley, C., & Raftery, A. (2002). Model-based clustering, discriminant analysis, and den-
774 sity estimation. *Journal of the American Statistical Association*, *97*(458), 611–631.
- 775 Furukawa, Y. (1993). Depth of the decoupling plate interface and thermal structure un-
776 der arcs. *Journal of Geophysical Research: Solid Earth*, *98*(B11), 20005–20013.
- 777 Gao, X., & Wang, K. (2014). Strength of stick-slip and creeping subduction megathrusts
778 from heat flow observations. *Science*, *345*(6200), 1038–1041.
- 779 Gerya, T. (2019). *Introduction to numerical geodynamic modelling*. Cambridge Univer-
780 sity Press.
- 781 Gerya, T., & Stöckhert, B. (2006). Two-dimensional numerical modeling of tectonic and
782 metamorphic histories at active continental margins. *International Journal of Earth*
783 *Sciences*, *95*(2), 250–274.
- 784 Gerya, T., & Yuen, D. (2003). Characteristics-based marker-in-cell method with con-
785 servative finite-differences schemes for modeling geological flows with strongly vari-
786 able transport properties. *Physics of the Earth and Planetary Interiors*, *140*(4), 293–
787 318.
- 788 Gerya, T., Stöckhert, B., & Perchuk, A. (2002). Exhumation of high-pressure metamor-
789 phic rocks in a subduction channel: A numerical simulation. *Tectonics*, *21*(6), 6–1.
- 790 Gerya, T., Connolly, J., & Yuen, D. (2008). Why is terrestrial subduction one-sided? *Ge-*
791 *ology*, *36*(1), 43–46.

- 792 Gorczyk, W., Willner, A., Gerya, T., Connolly, J., & Burg, J. (2007). Physical controls
 793 of magmatic productivity at pacific-type convergent margins: Numerical modelling.
 794 *Physics of the Earth and Planetary Interiors*, 163(1-4), 209–232.
- 795 Groppo, C., Rolfo, F., Sachan, H., & Rai, S. (2016). Petrology of blueschist from the west-
 796 ern himalaya (ladakh, NW india): Exploring the complex behavior of a lawsonite-
 797 bearing system in a paleo-accretionary setting. *Lithos*, 252, 41–56.
- 798 Hacker, B. (1996). Eclogite formation and the rheology, buoyancy, seismicity, and $h \sim 20$
 799 content of oceanic crust. *GEOPHYSICAL MONOGRAPH-AMERICAN GEOPHYS-*
 800 *ICAL UNION*, 96, 337–346.
- 801 Hacker, B. (2008). H₂O subduction beyond arcs. *Geochemistry, Geophysics, Geosystems*,
 802 9(3).
- 803 Hacker, B., Abers, G., & Peacock, S. (2003). Subduction factory 1. Theoretical miner-
 804 alogy, densities, seismic wave speeds, and H₂O contents. *Journal of Geophysical Re-*
 805 *search: Solid Earth*, 108(B1).
- 806 Harlow, F. (1962). *The particle-in-cell method for numerical solution of problems in fluid*
 807 *dynamics*. Los Alamos Scientific Lab., N. Mex.
- 808 Harlow, F. (1964). The particle-in-cell computing method for fluid dynamics. *Methods*
 809 *Comput. Phys.*, 3, 319–343.
- 810 Harlow, F., & Welch, J. (1965). Numerical calculation of time-dependent viscous incom-
 811 pressible flow of fluid with free surface. *The Physics of Fluids*, 8(12), 2182–2189.
- 812 Hilairret, N., Reynard, B., Wang, Y., Daniel, I., Merkel, S., Nishiyama, N., & Petitgirard,
 813 S. (2007). High-pressure creep of serpentine, interseismic deformation, and initiation
 814 of subduction. *Science*, 318(5858), 1910–1913.

- 815 Holt, A., & Condit, C. (2021). Slab temperature evolution over the lifetime of a subduc-
 816 tion zone. *Geochemistry, Geophysics, Geosystems*, e2020GC009476.
- 817 Hu, J., & Gurnis, M. (2020). Subduction duration and slab dip. *Geochemistry, Geophysics,*
 818 *Geosystems*, 21(4), e2019GC008862.
- 819 Hyndman, R., & Peacock, S. (2003). Serpentinization of the forearc mantle. *Earth and*
 820 *Planetary Science Letters*, 212(3-4), 417–432.
- 821 Hyndman, R., Currie, C., & Mazzotti, S. (2005). Subduction zone backarcs, mobile belts,
 822 and orogenic heat. *GSA Today*, 15(2), 4–10.
- 823 Ioannidi, P., Angiboust, S., Oncken, O., Agard, P., Glodny, J., & Sudo, M. (2020). De-
 824 formation along the roof of a fossil subduction interface in the transition zone below
 825 seismogenic coupling: The austroalpine case and new insights from the malenco mas-
 826 sif (central alps). *Geosphere*, 16(2), 510–532.
- 827 Ioannidi, P., Le Pourhiet, L., Agard, P., Angiboust, S., & Oncken, O. (2021). Effective
 828 rheology of a two-phase subduction shear zone: Insights from numerical simple shear
 829 experiments and implications for subduction zone interfaces. *Earth and Planetary*
 830 *Science Letters*, 566, 116913.
- 831 Ito, K., & Kennedy, G. (1971). An experimental study of the basalt-garnet granulite-
 832 eclogite transition. *The Structure and Physical Properties of the Earth's Crust*, 14,
 833 303–314.
- 834 Karato, S., & Wu, P. (1993). Rheology of the upper mantle: A synthesis. *Science*, 260(5109),
 835 771–778.
- 836 Kerswell, B., & Kohn, M. (2022). A comparison of surface heat flow interpolations near
 837 subduction zones. *Submitted to Geochemistry, Geophysics, Geosystems*.

- 838 Kerswell, B., Kohn, M., & Gerya, T. (2021). Backarc lithospheric thickness and serpen-
 839 tine stability control slab-mantle coupling depths in subduction zones. *Geochemistry,*
 840 *Geophysics, Geosystems, 22*(6), e2020GC009304.
- 841 Kitamura, Y., & Kimura, G. (2012). Dynamic role of tectonic mélange during interseis-
 842 mic process of plate boundary mega earthquakes. *Tectonophysics, 568*, 39–52.
- 843 Kohn, M. (2020). A refined zirconium-in-rutile thermometer. *American Mineralogist:*
 844 *Journal of Earth and Planetary Materials, 105*(6), 963–971.
- 845 Kohn, M., Castro, A., Kerswell, B., Ranero, C. R., & Spear, F. (2018). Shear heating
 846 reconciles thermal models with the metamorphic rock record of subduction. *Proceed-*
 847 *ings of the National Academy of Sciences, 115*(46), 11706–11711.
- 848 Kotowski, A., & Behr, W. (2019). Length scales and types of heterogeneities along the
 849 deep subduction interface: Insights from exhumed rocks on syros island, greece. *Geo-*
 850 *sphere, 15*(4), 1038–1065.
- 851 Locatelli, M., Federico, L., Agard, P., & Verlaguet, A. (2019). Geology of the southern
 852 monviso metaophiolite complex (w-alps, italy). *Journal of Maps, 15*(2), 283–297.
- 853 Mann, M., Abers, G., Daly, K., & Christensen, D. (2022). Subduction of an oceanic plateau
 854 across southcentral alaska: Scattered-wave imaging. *Journal of Geophysical Research:*
 855 *Solid Earth, e2021JB022697*.
- 856 McKenzie, D. (1969). Speculations on the consequences and causes of plate motions. *Geo-*
 857 *physical Journal International, 18*(1), 1–32.
- 858 Molnar, P., & England, P. (1990). Temperatures, heat flux, and frictional stress near ma-
 859 jor thrust faults. *Journal of Geophysical Research: Solid Earth, 95*(B4), 4833–4856.

- 860 Monie, P., & Agard, P. (2009). Coeval blueschist exhumation along thousands of kilo-
861 meters: Implications for subduction channel processes. *Geochemistry, Geophysics,*
862 *Geosystems, 10*(7).
- 863 Moresi, L., Dufour, F., & Mühlhaus, H. (2003). A lagrangian integration point finite el-
864 ement method for large deformation modeling of viscoelastic geomaterials. *Journal*
865 *of Computational Physics, 184*(2), 476–497.
- 866 Morishige, M., & Kuwatani, T. (2020). Bayesian inversion of surface heat flow in sub-
867 duction zones: A framework to refine geodynamic models based on observational con-
868 straints. *Geophysical Journal International, 222*(1), 103–109.
- 869 Naif, S., Key, K., Constable, S., & Evans, R. (2015). Water-rich bending faults at the
870 middle america trench. *Geochemistry, Geophysics, Geosystems, 16*(8), 2582–2597.
- 871 Okay, A. (1989). Alpine-himalayan blueschists. *Annual Review of Earth and Planetary*
872 *Sciences, 17*(1), 55–87.
- 873 Peacock, S. (1990). Fluid processes in subduction zones. *Science, 248*(4953), 329–337.
- 874 Peacock, S. (1996). Thermal and petrologic structure of subduction zones. *Subduction:*
875 *Top to Bottom, 96*, 119–133.
- 876 Peacock, S., & Wang, K. (1999). Seismic consequences of warm versus cool subduction
877 metamorphism: Examples from southwest and northeast japan. *Science, 286*(5441),
878 937–939.
- 879 Penniston-Dorland, S., Kohn, M., & Manning, C. (2015). The global range of subduc-
880 tion zone thermal structures from exhumed blueschists and eclogites: Rocks are hot-
881 ter than models. *Earth and Planetary Science Letters, 428*, 243–254.
- 882 Platt, J. (1986). Dynamics of orogenic wedges and the uplift of high-pressure metamor-
883 phic rocks. *Geological Society of America Bulletin, 97*(9), 1037–1053.

884 Plunder, A., Agard, P., Chopin, C., & Okay, A. (2013). Geodynamics of the tavşanlı zone,
 885 western turkey: Insights into subduction/obduction processes. *Tectonophysics*, *608*,
 886 884–903.

887 Plunder, A., Agard, P., Chopin, C., Pourteau, A., & Okay, A. (2015). Accretion, under-
 888 plating and exhumation along a subduction interface: From subduction initiation to
 889 continental subduction (tavşanlı zone, w. turkey). *Lithos*, *226*, 233–254.

890 Plunder, A., Thieulot, C., & Van Hinsbergen, D. (2018). The effect of obliquity on tem-
 891 perature in subduction zones: Insights from 3-d numerical modeling. *Solid Earth*, *9*(3),
 892 759–776.

893 Ranalli, G. (1995). *Rheology of the earth*. Springer Science & Business Media.

894 Reynolds, D. (2009). Gaussian mixture models. *Encyclopedia of Biometrics*, *741*, 659–
 895 663.

896 Roda, M., Marotta, A., & Spalla, M. (2010). Numerical simulations of an ocean-continent
 897 convergent system: Influence of subduction geometry and mantle wedge hydration
 898 on crustal recycling. *Geochemistry, Geophysics, Geosystems*, *11*(5).

899 Roda, M., Spalla, M., & Marotta, A. (2012). Integration of natural data within a nu-
 900 merical model of ablative subduction: A possible interpretation for the alpine dynam-
 901 ics of the austroalpine crust. *Journal of Metamorphic Geology*, *30*(9), 973–996.

902 Roda, M., Zucali, M., Regorda, A., & Spalla, M. (2020). Formation and evolution of a
 903 subduction-related mélange: The example of the rocca canavese thrust sheets (west-
 904 ern alps). *Bulletin*, *132*(3-4), 884–896.

905 Rondenay, S., Abers, G., & van Keken, P. (2008). Seismic imaging of subduction zone
 906 metamorphism. *Geology*, *36*(4), 275–278.

- 907 Ruh, J., Le Pourhiet, L., Agard, P., Burov, E., & Gerya, T. (2015). Tectonic slicing of
908 subducting oceanic crust along plate interfaces: Numerical modeling. *Geochemistry,*
909 *Geophysics, Geosystems, 16*(10), 3505–3531.
- 910 Schmidt, M., & Poli, S. (1998). Experimentally based water budgets for dehydrating slabs
911 and consequences for arc magma generation. *Earth and Planetary Science Letters,*
912 *163*(1-4), 361–379.
- 913 Schwarz, G. (1978). Estimating the dimension of a model. *The Annals of Statistics, 4*61–
914 464.
- 915 Scrucca, L., Fop, M., Murphy, T., & Raftery, A. (2016). Mclust 5: Clustering, classifi-
916 cation and density estimation using gaussian finite mixture models. *The R Journal,*
917 *8*(1), 289.
- 918 Shreve, R., & Cloos, M. (1986). Dynamics of sediment subduction, melange formation,
919 and prism accretion. *Journal of Geophysical Research: Solid Earth, 91*(B10), 10229–
920 10245.
- 921 Sizova, E., Gerya, T., Brown, M., & Perchuk, L. (2010). Subduction styles in the pre-
922 cambrian: Insight from numerical experiments. *Lithos, 116*(3-4), 209–229.
- 923 Soret, M., Bonnet, G., Agard, P., Larson, K., Cottle, J., Dubacq, B., et al. (2022). Timescales
924 of subduction initiation and evolution of subduction thermal regimes. *Earth and Plan-*
925 *etary Science Letters, 584,* 117521.
- 926 Spear, F., & Selverstone, J. (1983). Quantitative PT paths from zoned minerals: The-
927 ory and tectonic applications. *Contributions to Mineralogy and Petrology, 83*(3), 348–
928 357.
- 929 Stöckhert, B. (2002). Stress and deformation in subduction zones: Insight from the record
930 of exhumed metamorphic rocks. *Geological Society, London, Special Publications, 200*(1),
931 255–274.

- 932 Syracuse, E., & Abers, G. (2006). Global compilation of variations in slab depth beneath
 933 arc volcanoes and implications. *Geochemistry, Geophysics, Geosystems*, 7(5).
- 934 Syracuse, E., van Keken, P., Abers, G., Suetsugu, D., Bina, C., Inoue, T., et al. (2010).
 935 The global range of subduction zone thermal models. *Physics of the Earth and Plan-*
 936 *etary Interiors*, 183(1-2), 73–90.
- 937 Tewksbury-Christle, C., & Behr, W. (2021). Constraints from exhumed rocks on the seis-
 938 mic signature of the deep subduction interface. *Geophysical Research Letters*, 48(18).
- 939 Tewksbury-Christle, C., Behr, W., & Helper, M. (2021). Tracking deep sediment under-
 940 plating in a fossil subduction margin: Implications for interface rheology and mass
 941 and volatile recycling. *Geochemistry, Geophysics, Geosystems*, 22(3).
- 942 Turcotte, D., & Schubert, G. (2002). *Geodynamics*. Cambridge university press.
- 943 van Keken, P., Hacker, B., Syracuse, E., & Abers, G. (2011). Subduction factory: 4. Depth-
 944 dependent flux of H_2O from subducting slabs worldwide. *Journal of Geophysical Re-*
 945 *search*, 116(b1), b01401.
- 946 van Keken, P., Wada, I., Abers, G., Hacker, B., & Wang, K. (2018). Mafic high-pressure
 947 rocks are preferentially exhumed from warm subduction settings. *Geochemistry, Geo-*
 948 *physics, Geosystems*, 19(9), 2934–2961.
- 949 van Keken, P., Wada, I., Sime, N., & Abers, G. (2019). Thermal structure of the fore-
 950 arc in subduction zones: A comparison of methodologies. *Geochemistry, Geophysics,*
 951 *Geosystems*, 20(7), 3268–3288.
- 952 Vermeesch, P. (2018). IsoplotR: A free and open toolbox for geochronology. *Geoscience*
 953 *Frontiers*, 9(5), 1479–1493.

954 Wada, I., & Wang, K. (2009). Common depth of slab-mantle decoupling: Reconciling
955 diversity and uniformity of subduction zones. *Geochemistry, Geophysics, Geosystems*,
956 *10*(10).

957 Wakabayashi, J. (2015). Anatomy of a subduction complex: Architecture of the fran-
958 ciscan complex, california, at multiple length and time scales. *International Geology*
959 *Review*, *57*(5-8), 669–746.

960 Yamato, P., Agard, P., Burov, E., Le Pourhiet, L., Jolivet, L., & Tiberi, C. (2007). Burial
961 and exhumation in a subduction wedge: Mutual constraints from thermomechani-
962 cal modeling and natural p-t-t data (schistes lustrés, western alps). *Journal of Geo-*
963 *physical Research: Solid Earth*, *112*(B7).

964 Yamato, P., Burov, E., Agard, P., Le Pourhiet, L., & Jolivet, L. (2008). HP-UHP ex-
965 humation during slow continental subduction: Self-consistent thermodynamically and
966 thermomechanically coupled model with application to the western alps. *Earth and*
967 *Planetary Science Letters*, *271*(1-4), 63–74.

968 **A Appendix**

969 **A.1 Gaussian Mixture Models**

Let the traced markers represent a d -dimensional array of n random independent variables $x_i \in \mathbb{R}^{n \times d}$. Assume markers x_i were drawn from k discrete probability distributions with parameters Φ . The probability distribution of markers x_i can be modeled with a mixture of k components:

$$p(x_i|\Phi) = \sum_{j=1}^k \pi_j p(x_i|\Theta_j) \quad (\text{A.1})$$

970 where $p(x_i|\Theta_j)$ is the probability of x_i under the j^{th} mixture component and π_j is the
 971 mixture proportion representing the probability that x_i belongs to the j^{th} component
 972 ($\pi_j \geq 0$; $\sum_{j=1}^k \pi_j = 1$).

Assuming Θ_j describes a Gaussian probability distributions with mean μ_j and covariance Σ_j , Equation (A.1) becomes:

$$p(x_i|\Phi) = \sum_{j=1}^k \pi_j \mathcal{N}(x_i|\mu_j, \Sigma_j) \quad (\text{A.2})$$

where

$$\mathcal{N}(x_i|\mu_j, \Sigma_j) = \frac{\exp\{-\frac{1}{2}(x_i - \mu_j)(x_i - \mu_j)^T \Sigma_j^{-1}\}}{\sqrt{\det(2\pi \Sigma_j)}} \quad (\text{A.3})$$

The parameters μ_j and Σ_j , representing the center and shape of each cluster, are estimated by maximizing the log of the likelihood function, $L(x_i|\Phi) = \prod_{i=1}^n p(x_i|\Phi)$:

$$\log L(x_i|\Phi) = \log \prod_{i=1}^n p(x_i|\Phi) = \sum_{i=1}^n \log \left[\sum_{j=1}^k \pi_j p(x_i|\Theta_j) \right] \quad (\text{A.4})$$

Taking the derivative of Equation (A.4) with respect to each parameter, π , μ , Σ , setting the equation to zero, and solving for each parameter gives the maximum likelihood estimators:

$$\begin{aligned} N_j &= \sum_{i=1}^n \omega_i \\ \pi_j &= \frac{N_j}{n} \\ \mu_j &= \frac{1}{N_j} \sum_{i=1}^n \omega_i x_i \\ \Sigma_j &= \frac{1}{N_j} \sum_{i=1}^n \omega_i (x_i - \mu_j)(x_i - \mu_j)^T \end{aligned} \quad (\text{A.5})$$

973 where ω_i ($\omega_i \geq 0$; $\sum_{j=1}^k \omega_i = 1$) are membership weights representing the probability
 974 of an observation x_i belonging to the j^{th} Gaussian and N_j represents the number of ob-
 975 servations belonging to the j^{th} Gaussian. Please note that ω_i is unknown for markers
 976 so maximum likelihood estimator cannot be computed with Equation (A.5). The solu-
 977 tion to this problem is the Expectation-Maximization algorithm, which is defined below.

General purpose functions in the R package `Mclust` (Scrucca et al., 2016) are used
 to fit Gaussian mixture models. “Fitting” refers to adjusting all k Gaussian parameters
 μ_j and Σ_j until the data and Gaussian ellipsoids achieve maximum likelihood defined
 by Equation (A.4). After Banfield & Raftery (1993), covariance matrices Σ in `Mclust`
 are parameterized to be flexible in their shape, volume, and orientation (Scrucca et al.,
 2016):

$$\Sigma_j = \lambda_j D_j A_j D_j^T \quad (\text{A.6})$$

978 where D_j is the orthogonal eigenvector matrix, A_j and λ_j are diagonal matrices of val-
 979 ues proportional to the eigenvalues. This implementation allows fixing one, two, or three
 980 geometric elements of the covariance matrices. That is, the volume λ_j , shape A_j , and
 981 orientation D_j of Gaussian clusters can change or be fixed among all k clusters (e.g. Celeux
 982 & Govaert, 1995; Fraley & Raftery, 2002). Fourteen parameterizations of Equation (A.6)
 983 are tried, representing different geometric combinations of the covariance matrices Σ (see
 984 Scrucca et al., 2016) and the Bayesian information criterion is computed (Schwarz, 1978).
 985 The parameterization for Equation (A.6) is chosen by Bayesian information criterion.

986 **A.2 Expectation-Maximization**

987 The Expectation-Maximization algorithm estimates Gaussian mixture model pa-
 988 rameters by initializing k Gaussians with parameters (π_j, μ_j, Σ_j) , then iteratively com-
 989 puting membership weights with Equation (A.7) and updating Gaussian parameters with
 990 Equation (A.5) until reaching a convergence threshold (Dempster et al., 1977).

The *expectation* (E-)step involves a “latent” multinomial variable $z_i \in \{1, 2, \dots, k\}$
 representing the unknown classifications of x_i with a joint distribution $p(x_i, z_i) = p(x_i|z_i)p(z_j)$.
 Membership weights ω_i are equivalent to the conditional probability $p(z_i|x_i)$, which rep-
 represents the probability of observation x_i belonging to the j^{th} Gaussian. Given initial guesses
 for Gaussian parameters π_j, μ_j, Σ_j , membership weights are computed using Bayes The-

orem (E-step):

$$p(z_i|x_i) = \frac{p(x_i|z_i)p(z_i)}{p(x_i)} = \frac{\pi_j \mathcal{N}(\mu_j, \Sigma_j)}{\sum_{j=1}^k \pi_j \mathcal{N}(\mu_j, \Sigma_j)} = \omega_i \quad (\text{A.7})$$

991 and Gaussian estimates are updated during the *maximization* (M-)step by applying ω_i
 992 to Equation (A.5). This step gives markers x_i class labels $z_i \in \{1, \dots, k\}$ representing
 993 assignment to one of k clusters (Figure 2).